

Systematic biases from the exclusion of higher harmonics in parameter estimation on LISA binaries

Sophia Yi ^{1,*} Francesco Iacovelli ^{1,†} Sylvain Marsat ^{2,‡} Digvijay Wadekar ^{1,§} and Emanuele Berti ^{1,¶}

¹*William H. Miller III Department of Physics and Astronomy,
Johns Hopkins University, 3400 North Charles Street, Baltimore, Maryland, 21218, USA*

²*Laboratoire des 2 Infinis - Toulouse (L2IT-IN2P3),
Université de Toulouse, CNRS, UPS, F-31062 Toulouse Cedex 9, France*

(Dated: February 19, 2025)

The remarkable sensitivity achieved by the planned Laser Interferometer Space Antenna (LISA) will allow us to observe gravitational-wave signals from the mergers of massive black hole binaries (MBHBs) with signal-to-noise ratio (SNR) in the hundreds, or even thousands. At such high SNR, our ability to precisely infer the parameters of an MBHB from the detected signal will be limited by the accuracy of the waveform templates we use. In this paper, we explore the systematic biases that arise in parameter estimation if we use waveform templates that do not model radiation in higher-order multipoles. This is an important consideration for the large fraction of high-mass events expected to be observed with LISA. We examine how the biases change for MBHB events with different total masses, mass ratios, and inclination angles. We find that systematic biases due to insufficient mode content are severe for events with total redshifted mass $\gtrsim 10^6 M_\odot$. We then compare several methods of predicting such systematic biases without performing a full Bayesian parameter estimation. In particular, we show that through direct likelihood optimization it is possible to predict systematic biases with remarkable computational efficiency and accuracy. Finally, we devise a method to construct approximate waveforms including angular multipoles with $\ell \geq 5$ to better understand how many additional modes (beyond the ones available in current approximants) might be required to perform unbiased parameter estimation on the MBHB signals detected by LISA.

I. INTRODUCTION

As the catalog of gravitational wave (GW) events grows and the detectors improve in sensitivity, our ability to characterize the properties of individual events and of compact binary populations will be increasingly limited by systematic effects. Some of these systematic effects are due to detector noise and astrophysics, but waveform systematics are particularly important, and they have attracted a significant amount of attention in the context of ground-based detectors (see e.g. [1–15]).

The Laser Interferometer Space Antenna (LISA) is expected to observe binary black holes (BBHs) with much larger total masses and mass ratios, and with considerably louder signal-to-noise ratios (SNRs), than anything we have seen thus far in ground-based observatories (see e.g. Refs. [16, 17]). It has long been recognized that systematic biases in waveform modeling could be considerably worse for parameter estimation (PE) with signals detected by LISA [18–21]. Thus far, however, little work has been done to attempt to understand just how significant these biases will be, and how they may vary across the parameter space.

One source of systematic bias expected to affect PE with LISA sources is the bias due to neglecting higher

harmonics in waveforms. It has been known for some time that more energy is radiated in higher multipoles for systems with larger mass ratios [22], and that the inclusion of higher multipoles will significantly enhance the science return of ringdown observations with LISA [23–25].

Numerous authors have studied the biases introduced by neglecting higher-order modes in PE on BBH signals in current ground-based observatories, generally finding significant systematic errors due to the omission of higher modes for systems with high mass ratio, large total mass, high SNR, and inclination angle close to $\pi/2$ (edge-on systems) [26–32]. Some of these and other works have additionally found that relying on quadrupole-only waveforms decreases the efficacy of searches for BBH systems in current ground-based detectors, again in particular for heavier, more asymmetric, and more edge-on binaries [33–35]. A recent series of papers found that a combination of downweighting glitches and including higher modes in searches of the data of the third observing run of LIGO resulted in 14 new BBH event candidates, in addition to increasing the significance of several candidates previously deemed “marginal” [36–38], as well as increasing the overall sensitive volume of GW searches [39]. On the other hand, another recent study found that the exclusion of higher harmonics caused relatively minimal biases in parametrized post-Einsteinian (ppE) tests of general relativity, at least compared to the biases induced by other neglected physics (i.e., precession) [15]. However, it is unclear how this result would extend to considerably more massive events. There is clearly motivation to account for higher modes more carefully, both in detection and in PE with GW signals. In this study, we will focus on the

* syi24@jh.edu

† fiacovelli@jhu.edu

‡ sylvain.marsat@l2it.in2p3.fr

§ jayw@jhu.edu

¶ berti@jhu.edu

importance of subdominant modes in performing PE on BBHs observed by LISA.

One previous study [40] demonstrated that, when performing PE on a high-SNR massive black hole binary (MBHB) event of the kind anticipated to be observed with LISA, systematic biases arise due to insufficient mode content in the waveform templates used for signal recovery. This phenomenon was demonstrated explicitly in Ref. [40] for a single example binary. In this paper, we perform the same analysis of varying the mode content in waveform templates for several example MBHB systems, studying how the aforementioned systematic biases in PE change for events with different total masses, mass ratios, and inclination angles. We then investigate the extent to which these biases can be predicted in a cost-efficient manner, i.e., without having to perform PE for every MBHB event under consideration. We use one such method (direct likelihood optimization; see Sec. II C), which we find to be remarkably accurate in estimating systematic biases, to set approximate boundaries on the parameter space in which unbiased PE can be performed (i.e., where there is no significant bias due to neglecting a higher-order mode in the waveform template).

In Fig. 1 we show some results of this approximate boundary-setting for biases on the intrinsic parameters

$$\begin{aligned} \mathcal{M}_c &= \frac{(m_1 m_2)^{3/5}}{(m_1 + m_2)^{1/5}}, \\ q &= m_1/m_2 > 1, \\ \chi_{\pm} &= \frac{m_1 \chi_1 \pm m_2 \chi_2}{m_1 + m_2}, \end{aligned} \quad (1)$$

where m_1, m_2 and χ_1, χ_2 are the individual masses and dimensionless spins of the progenitor BHs, respectively. For each bin in the grid of detector-frame total mass $M/M_{\odot} \in [3 \times 10^5, 10^6]$ and mass ratio $q \in [1.1, 10]$, we show the minimum redshift at which the systematic bias on parameters $[\mathcal{M}_c, q, \chi_+, \chi_-]$ due to excluding the $(\ell, m) = (3, 2)$ mode is still less than the 2σ statistical error on the parameter. Results are shown for systems with inclination angle $\iota = \pi/3$. Moving from left to right in the plot, we see that biases initially become worse as we move toward more massive and more asymmetric binaries, as expected. Continuing further, we have the balancing effect of the chirp mass decreasing going from top left to bottom right, such that mergers occur at higher frequencies. When the merger, where higher-order modes are most important, is pushed toward the higher-frequency region where LISA is less sensitive, the bias due to neglecting these modes becomes less severe again. The reason for the chosen range of total mass (y -axis) will be clear in Sec. III, where we find that our PE results on MBHB events with total mass $\lesssim 3 \times 10^5 M_{\odot}$ do not exhibit significant biases, whereas the PE for events with total mass $\sim 10^6 M_{\odot}$ is significantly biased. Details on the construction of Fig. 1, as well as similar plots for extrinsic parameters and for systems with inclination $\iota \approx \pi/2$, are given in Sec. V B.

In the following sections, we lay out the components

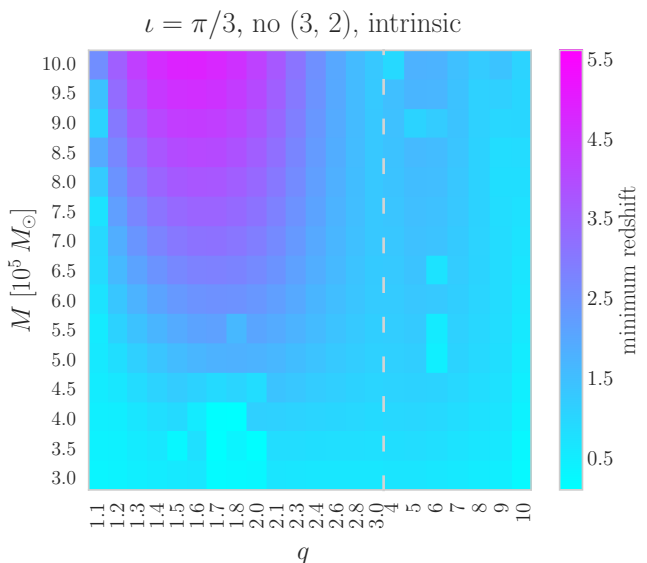


FIG. 1. Minimum redshift at which parameter estimation is unbiased, in the sense that the systematic bias on all four intrinsic parameters \mathcal{M}_c , q , χ_+ , and χ_- due to neglecting the $(\ell, m) = (3, 2)$ mode in the waveform template is less than the 2σ statistical error on the parameters. For example, for $M = 7 \times 10^5 M_{\odot}$ and $q = 2$ the parameter estimation is biased when $z \lesssim 3$. The grid is log-spaced between $q \in [1.1, 3]$ and spaced linearly between $q \in [3, 10]$ (with the transition marked by the dashed gray line), due to the more significant changes in results observed as we move from nearly symmetric to clearly asymmetric binaries. The corresponding plot for extrinsic parameters (sky localization and distance) is given in Fig. 14.

that go into the construction and interpretation of Fig. 1. In Sec. II, we outline how we perform both full PE with `lisabeta` [41] and several cheaper methods of estimating systematic bias. In Secs. III and IV, we show the results of PE for the intrinsic and extrinsic parameters of about 20 selected binaries, respectively. In Sec. V, we show how our methods of rapidly approximating bias compare to PE and present more plots similar to Fig. 1. Finally, in Sec. VI, we show the results of performing PE with crude waveforms containing more higher-order modes than are currently modeled with the waveform approximants we use for PE (IMRPHENOMXHM [42]). Throughout this paper we use geometrical units ($G = c = 1$).

II. METHODOLOGY

A. Parameter estimation with `lisabeta`

We examine the extent of systematic biases due to incomplete mode content in the GW templates used for PE on MBHBs of the kind expected to be observed by LISA. We use `lisabeta` [41] to perform PE varying the redshifted total mass ($M/M_{\odot} = 10^5, 10^6$), mass ratio ($q = 1.1, 4, 8$), and inclination angle ($\iota = \pi/12, \pi/3, \pi/2 -$

TABLE I. Parameters of the MBHB sources on which we perform PE with a varying number of modes. The value of D_L is chosen to correspond to $z = 1$. For the BBHs with total mass $3 \times 10^5 M_\odot$, we only run PE at the median inclination angle ($\iota = \pi/3$).

Parameter	Values
$M (M_\odot)$	$10^5, 3 \times 10^5, 10^6$
q	1.1, 4, 8
$\chi_{1,2}$	0
D_L (Mpc)	6791.81
t_c (s)	0.0
β_L (rad)	$\pi/6$
λ_L (rad)	1.8
ϕ (rad)	0.2
Ψ_L (rad)	1.2
ι (rad)	$\pi/12, \pi/3, \pi/2 - \pi/12$

$\pi/12$). Observing stark differences in the results for events with total mass $10^5 M_\odot$ vs. $10^6 M_\odot$, we also run PE on a few additional events at the intermediate mass of $3 \times 10^5 M_\odot$, with the median inclination angle ($\iota = \pi/3$). Altogether, this amounts to a total of 21 PE runs with `lisabeta`. The rest of the parameters (not modified between runs) are listed in Table I, where $\chi_{1,2}$ are the dimensionless progenitor spins aligned with the orbital angular momentum of the binary; D_L is the luminosity distance in Mpc, which we choose to correspond to redshift $z = 1$; and t_c is the time of coalescence. The angles β_L and λ_L are the ecliptic latitude and longitude, respectively, in the LISA frame; ϕ is BBH source frame phase; and Ψ_L is the polarization in the LISA frame.

For each combination of parameters, we generate the injected waveform for the event with the IMRPHENOMXHM waveform model [42, 43], including the $(\ell, m) = (2, 2), (2, 1), (3, 3), (3, 2)$ and $(4, 4)$ modes – i.e., all the available modes with the IMRPHENOMXHM waveform approximant. (From here on, whenever we denote a mode by a comma-delimited pair of numbers in parentheses, we will be referring to the angular harmonic indices of the mode, as done here.) We then perform PE on the signal with `lisabeta` using first a template with all five modes, then we iterate with one less mode, until we are attempting to recover the signal with just the quadrupole. The authors of Ref. [40] chose to “deactivate” modes in order of SNR contribution, such that a four-mode template excludes only the mode with the lowest SNR, the three-mode template excludes the two “quietest” modes, etc. To simplify comparisons between our different events, we always include modes in the following order:

- 1 mode: (2, 2)
- 2 modes: (2, 2), (3, 3)
- 3 modes: (2, 2), (3, 3), (2, 1)
- 4 modes: (2, 2), (3, 3), (2, 1), (4, 4)
- 5 modes: (2, 2), (3, 3), (2, 1), (4, 4), (3, 2)

This ordering was chosen for a number of reasons.

First, when examining the mode-by-mode SNR of the 21 events we considered, 9 out of the 21 exhibited the above ordering. In Fig. 2, we can see the prevalence of this mode ordering within the region of parameter space we consider. For each inclination angle, different colors indicate a different ordering of the subdominant modes (ranked from “loudest” to “quietest”). In all the configurations shown here, the (2, 2) mode dominates, with the (3, 3) mode generally being the second loudest. The ordering of the (2, 1), (4, 4), and (3, 2) modes varies a bit more, with the (4, 4) usually being the quietest for a nearly face-on system, and the (3, 2) generally being the quietest otherwise.

Second, although the odd- m modes are suppressed for events with $q \approx 1$ (in the case of non-spinning progenitors, which we consider here), we find that templates with $m \neq 2$ nevertheless perform better in breaking degeneracies observed with (2, 2)-only templates. This is due to the fact that modes with the same azimuthal number m (e.g., the (2, 2) and (3, 2)) share the same orbital phasing, whereas modes with different m ’s exhibit a different phasing behavior that cannot be reproduced by the (2, 2). Therefore PE results can be improved with the addition of the (3, 3) or (2, 1) as the second mode after the (2, 2), despite these potentially being more “quiet” (i.e., having lower SNR) than the (3, 2) mode.

Lastly, mode mixing makes the differentiability of the IMRPHENOMXHM waveforms less clean for the (3, 2) mode. This makes it challenging to perform certain cost-efficient bias estimates which involve derivatives of the waveform. For this reason it is advantageous to include this mode last, in order to minimize unwanted effects on the results of these cheaper methods for events with less than 5 modes.

We use the power spectral density (PSD) required by the LISA Science Requirements Document (SciRDv1) [44]. We assume the frequency range of LISA to be 10^{-5} –0.5 Hz and incorporate the full response of LISA [45]. We also account for a background of white dwarf noise as in Sec. 9 of Ref. [44].

To sample the GW likelihood, we use the parallel-tempered Markov chain Monte Carlo (MCMC) ensemble sampler `ptemcee` [46–48], which is a fast sampler well-adapted to handling complex posteriors. To improve the robustness for degenerate posteriors, the ensemble sampler is enriched with jump proposals designed to explore the possible sky multimodality [41]. For a typical PE run, we use 64 walkers and run `ptemcee` at 10 temperatures with a max temperature of 100. For each event, we sample in the combinations of mass and spin parameters $[\mathcal{M}_c, q, \chi_+, \text{ and } \chi_-]$ defined in Eq. (1). At first order in post-Newtonian (PN) theory, the GW frequency evolution is solely dependent on the chirp mass \mathcal{M}_c , so this is often the mass parameter that is most easily determined from the data. Similarly, χ_+ (also commonly known as χ_{eff}) is generally much easier to determine from the data than the individual spins χ_1 and χ_2 . Lastly, q and χ_- are

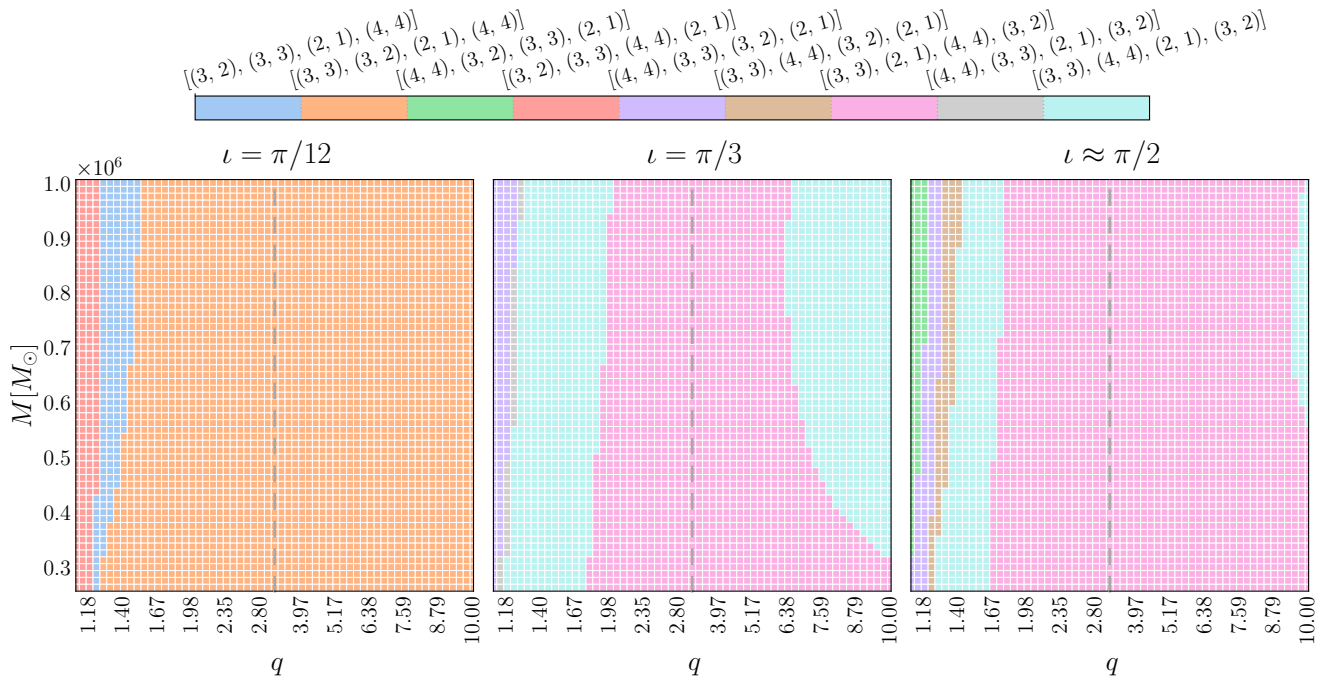


FIG. 2. Ordering of the subdominant modes by SNR contribution. The (2, 2) mode is always the dominant one. Each color corresponds to the subdominant multipole ordering that we observe within this region of parameter space; in the legend, the multipoles are ranked by SNR. For example, the pink region corresponds to the ordering (2, 2), (3, 3), (2, 1), (4, 4), (3, 2).

chosen to complete the set of mass and spin parameters, respectively.

To perform PE, we first calculate the Fisher covariance matrix and initialize chains from the results of this calculation. We set uniform priors on the chirp mass and distance in the range of 0.1 to 10 times their injected values. For the mass ratio, we use a uniform prior over the range [1, 10], and the spin parameters have a uniform prior over their allowed ranges of $[-1, 1]$.

B. Predicting biases in the linear signal approximation

Given the computational cost of full Bayesian PE analyses, it is desirable to have a much faster, cheaper method of predicting systematic biases due to, e.g., neglecting higher-order modes. One technique for accomplishing this is to estimate systematic errors in the linear signal approximation as done by Cutler & Vallisneri (henceforth, “CV”) in Ref. [19]. In Ref. [49], the errors calculated in this approximation were found to reliably predict the biases in parameter inference of ET and LISA sources due to overlapping signals, foregrounds created by unfitted sources, and incorrectly removed sources, among other things. The authors of Ref. [40] examined the usefulness of this technique for the example binary they considered, finding that the errors were not properly reconstructed within the linear signal approximation. Here we expand the study of the usefulness of the CV estimates, covering

a much larger region of parameter space than previously covered in Ref. [40]. In App. B, for completeness, we review the CV formalism. In Sec. V below we compare our PE results with the errors predicted by the CV estimates.

C. Predicting biases with direct likelihood optimization

In Sec. V we will confirm the finding of Ref. [40]: the biases due to neglecting higher-order modes are not always well-approximated via the CV formalism, in particular for more massive events. Given this result, it is desirable to explore other methods of predicting the biases we see in PE. In this section, we leverage the fact that the systematic bias we consider here is, by definition, the difference between the “true” (or injected) parameters and the parameters evaluated at the maximum likelihood given our best-fit waveform. Studying this bias, therefore, in principle reduces to a straightforward optimization problem. Indeed, in theory, performing a rigorous sampling from the posteriors might be considered excessive if one is only interested in studying the distance between the maximum likelihood point and the injection (assuming that the maximum likelihood point can be found without a sampler).

We will see in Sec. V that, just as expected, one can indeed infer the systematic bias with remarkable success when simply optimizing the likelihood directly. In this work, we use the Nelder-Mead algorithm [50] to maximize

the likelihood. Essentially, in the Nelder-Mead algorithm, a “simplex” with $n+1$ vertices (n being the number of variables) is introduced in the parameter space. The function value is evaluated at each vertex, and then the simplex systematically rearranges (growing, reflecting, contracting, etc.) such that it moves toward and eventually closes in on the location of the minimum. One appealing characteristic of this algorithm is that it is able to minimize a function of n variables without differentiation.

In this work, we use the implementation of the Nelder-Mead algorithm provided in `scipy` [51]. We initialize our simplex in $(n+1)$ -dimensional space by setting each vertex of the initial simplex at the likelihood evaluated with one parameter set to a value $m\sigma$ away from its injected value, where σ is calculated from the diagonal elements of the Fisher covariance matrix. We then minimize the function $-\ln(\mathcal{L})$ (i.e., we find the maximum likelihood). To accommodate the large range in parameter values (considering, for example, that we have masses $\mathcal{O}(10^5 - 10^6) M_\odot$ and angles in the range $[-\pi, \pi]$), we rescale parameters by the σ 's calculated from the Fisher analysis to perform this minimization. During the maximization procedure, we enforce the same prior boundaries on the parameters used in PE.

After using the Nelder-Mead algorithm to compute the location of the maximum likelihood a single time, we then take the location of this calculated maximum as an initial guess for the subsequent iteration of the algorithm, allowing the algorithm to determine the initial simplex based on this initial guess. We repeat this process until we find convergence. We find some dependence on the “size” of the initial simplex (m), as we will discuss in Sec. V. Generally, we find good performance with a rather broad initial simplex, i.e., setting something like $m = 20$. This suggests that, given the high dimensionality of the problem and the potential presence of multiple local minima throughout the parameter space, the algorithm performs best when the initial simplex is large enough to enclose the global minimum, which apparently does not necessarily coincide with the injected value, especially for the angles.

As we will see in Sec. V, we find that the parameters evaluated at the maximum likelihood found by the Nelder-Mead algorithm generally show good agreement with the median values of the posterior distributions recovered by a full Bayesian PE. In the few cases where the agreement is not very good, we attempted to see if the Nelder-Mead algorithm mistakenly finds incorrect (local) minima. To check this, we utilize the “Basin-hopping” technique as implemented in `scipy`, which attempts to find the global minimum by allowing the algorithm to “hop” between different regions of parameter space and explore the various local minima it encounters. We find that Basin-hopping generally does not improve the results of the optimization, suggesting that the Nelder-Mead algorithm is generally successful in finding the global minimum.

Importantly, we find that the biases can be estimated by directly maximizing the likelihood in this manner for

all 5 mode configurations for a given event in as little as 9 seconds to ~ 1 minute in a `Jupyter Notebook` running on a single core of an 8-core CPU (8GB memory). This is dramatically faster than the PE runs, which take $\sim 3 - 15$ minutes *per mode configuration* when parallelized across 48 cores (3.9GB RAM per CPU).

In Sec. V, we show how directly optimizing the likelihood with the Nelder-Mead algorithm can result in much better estimates of systematic biases than we are able to obtain with the CV formalism.

III. RESULTS: PARAMETER ESTIMATION WITH LISABETA

We now present PE results across our grid of parameter space, examining how biases arise due to an insufficient number of modes. In this section, we focus on examining the biases in intrinsic parameter recovery. Corresponding discussions for extrinsic parameters are given in Sec. IV. For simplicity, we restrict our analysis to injected signals with non-spinning progenitors ($\chi_1 = \chi_2 = 0$). We place our events at a distance corresponding to $z = 1$. For the rest of the extrinsic parameters (source localization, etc.), which we expect to have a minimal impact on our analysis, we simply take the arbitrary values listed in Table I.

A. Lowest mass events ($M = 10^5 M_\odot$)

We begin with results for the lowest-mass MBHBs, with total redshifted mass equal to $10^5 M_\odot$. The total SNRs of the events investigated in this section range from 188.6 to 692.7.

1. Events with $q = 1.1$

The first set of events with $M = 10^5 M_\odot$ that we examine have mass ratio $q = 1.1$ and differ in inclination angle $\iota = [\pi/12, \pi/3, \pi/2 - \pi/12]$. The posteriors on the intrinsic parameters \mathcal{M}_c, q, χ_+ , and χ_- generated for these events are presented in Fig. 3. The colors correspond to posteriors obtained with a different number of modes in the template used for recovery, as indicated in the legends. The top labels of the 1D histograms display the median values recovered with the *quadrupole-only* templates, which are generally the most biased values.

In general, we see that the posteriors close in more tightly around the injected values (marked by the black lines) when more modes are included in the template. For the nearly edge-on system ($\iota \approx \pi/2$) and the system with median inclination ($\iota = \pi/3$), the posteriors on the spin parameters χ_+ and χ_- are rather broad when inferred with only 1- or 2-mode templates. Nevertheless, the posteriors still peak around the correct (injected) value, and there are in general no strong biases.

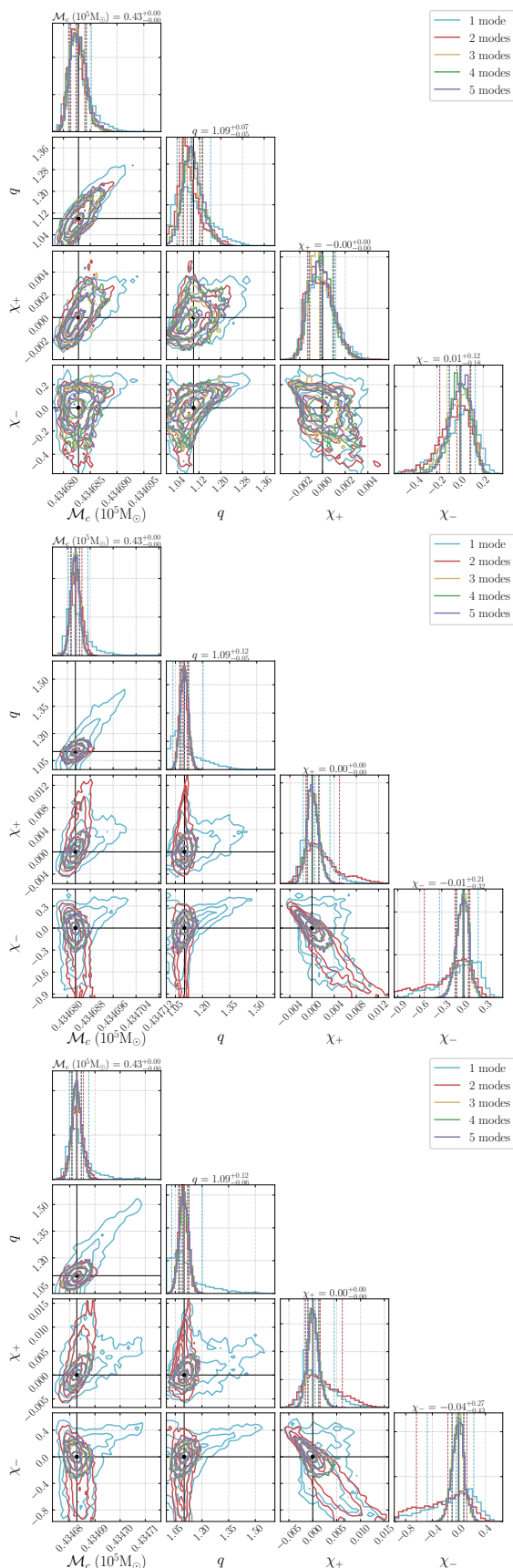


FIG. 3. $M = 10^5 M_\odot$, $q = 1.1$. Top, center, bottom: inclination angle and total SNR vary from $\iota = [\pi/12, \pi/3, \pi/2 - \pi/12]$ and $[692.7, 404.1, 298.4]$.

2. Events with $q = 4$

Next, we consider $M = 10^5 M_\odot$ events with $q = 4$, again varying the inclination angles. The results are presented in Fig. 4.

Compared with the approximately equal-mass events in Sec. III A 1, the posteriors are considerably more tightly centered around the true values. Moreover, there do not seem to be significant biases even for the spins. In fact, the posteriors in Fig. 4 look about the same across all 5 mode configurations, with the exception that using the 1-mode template can result in slightly broader posteriors.

This result may reflect the fact that, despite higher-order modes being more significant for more asymmetric binaries (larger q), with a larger q there is also comparatively more SNR in the inspiral compared to the merger/post-merger, where higher-order modes are most important. This could be a significant balancing effect for this set of lowest-mass events, for which higher modes are pushed to the high-frequency region of lower sensitivity of LISA. Moreover, note that the signal amplitude for a fixed total mass, and thus the SNR, decreases with increasing q .

3. Events with $q = 8$

The last set of $M = 10^5 M_\odot$ events we consider have mass ratio $q = 8$ and posterior distributions shown in Fig. 5. The results are quite similar to those shown in Fig. 4, i.e., there are no significant biases and somewhat tighter constraints on parameters than was observed in Fig. 3.

To summarize Secs. III A 1–III A 3, we see that the biases on the intrinsic parameters for this set of lowest-mass binaries are fairly negligible, and are certainly much less severe than the biases observed for the considerably heavier MBHB system examined in Ref. [40].

B. MBHBs with $M = 10^6 M_\odot$

We now consider events with $M = 10^6 M_\odot$. We will see that, as expected, the biases from insufficient mode content in the templates are more significant for these more massive events, which have total SNR in the range of 873.1 – 4105.2, compared to the much lower SNRs observed in Sec. III A.

1. Events with $q = 1.1$

Beginning with the nearly equal-mass events (see Fig. 6), we observe significant biases in parameter recovery with less than five modes in the template. We note that for the nearly face-on event, the posteriors on the chirp mass and spin parameters recovered by the (2, 2)-only template are all closer to the injected value

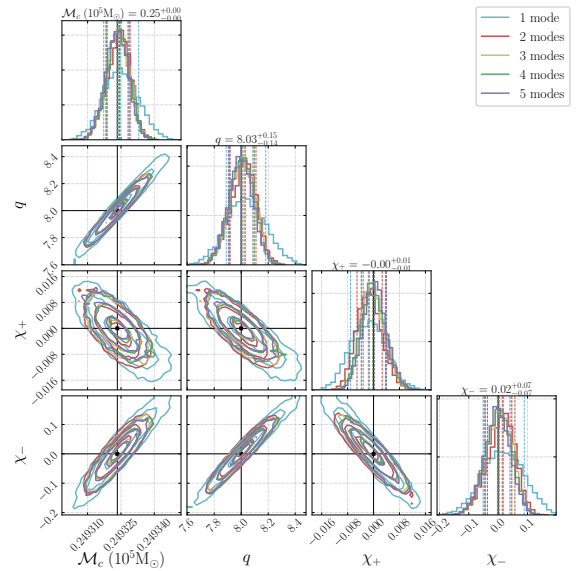
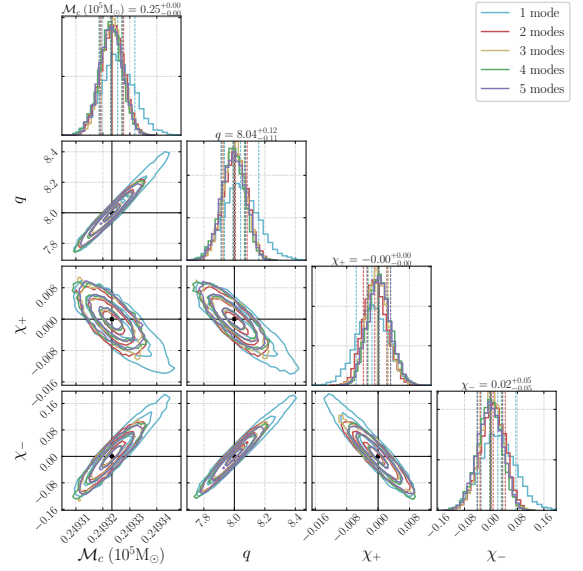
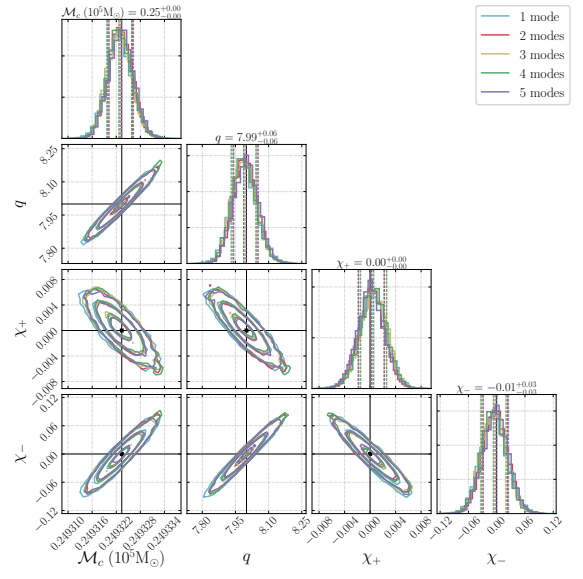
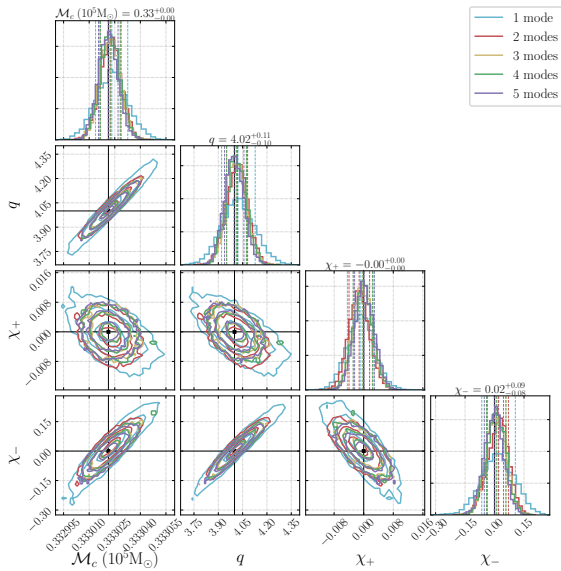
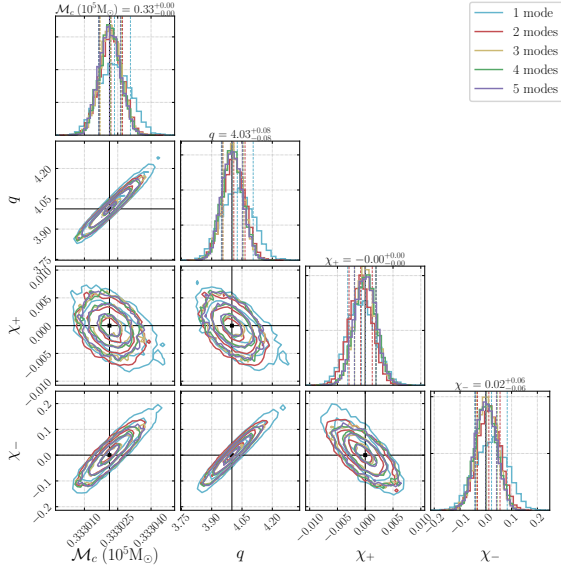
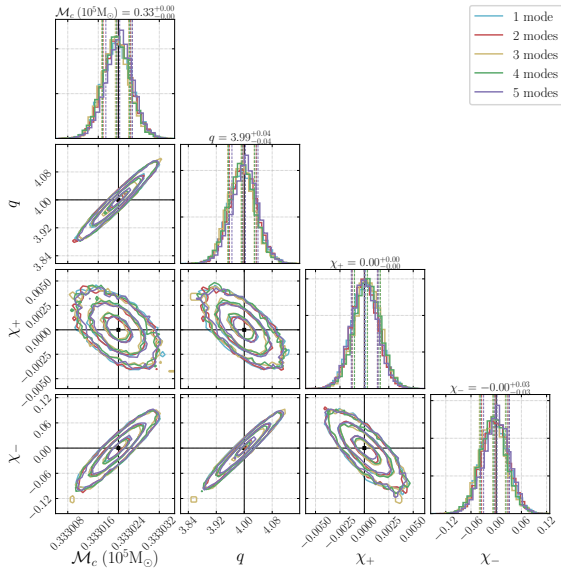


FIG. 4. $M = 10^5 M_\odot$, $q = 4$. Top, center, bottom: inclination angle and total SNR vary in the range $\iota = [\pi/12, \pi/3, \pi/2 - \pi/12]$ and $[551.8, 323.4, 238.9]$.

FIG. 5. $M = 10^5 M_\odot$, $q = 8$. Top, center, bottom: inclination angle and total SNR vary in the range $\iota = [\pi/12, \pi/3, \pi/2 - \pi/12]$ and $[433.7, 255.1, 188.6]$.

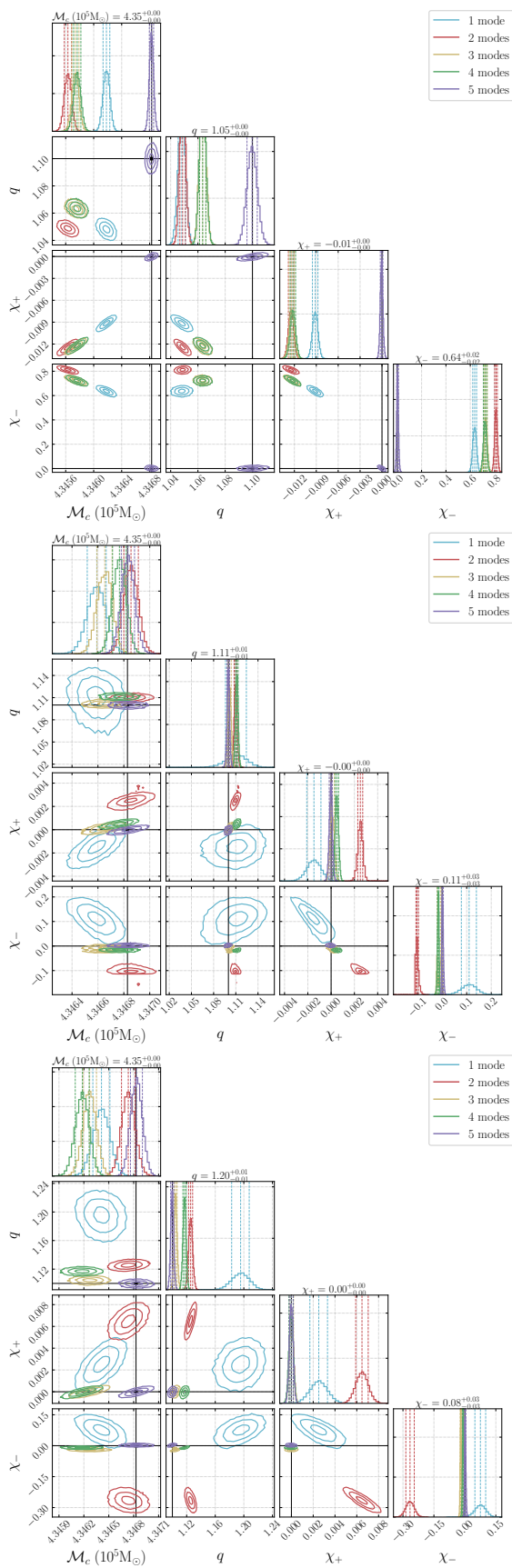


FIG. 6. $M = 10^6 M_\odot$, $q = 1.1$, $\iota = [\pi/12, \pi/3, \pi/2 - \pi/12]$, total SNR = [4105.2, 2317.3, 1678.3].

than posteriors with 2, 3, and 4 modes. This is a feature we also see in the nearly face-on events with other mass ratios (see top panels of Figs. 7 and 8). We recall that at inclinations close to zero, the radiation is overwhelmingly in the quadrupole, with additional modes (particularly the $m \neq 2$ modes) being very subdominant.

For the events with other inclination angles, parameter recovery with just the quadrupole is again sometimes apparently less biased than recovery with at least two modes; however, the posteriors are also considerably broader with the 1-mode template.

2. Events with $q = 4$

Compared to the $M = 10^6 M_\odot$, $q = 1.1$ events, the width of the posteriors for events with $q = 4$ shown in Fig. 7 is generally more consistent across different mode configurations. Here, we see the expected trend a bit more clearly for the $\iota = \pi/3$ and $\iota \approx \pi/2$ events, in the sense that the 1-mode template generally results in more biased posteriors than templates with more modes. For the $\iota = \pi/12$ event, we again see that the quadrupole-only template can perform better than templates with 2, 3, and 4 modes, particularly in recovering the injected values for M_c and q . Again, this could be a consequence of the fact that the (2, 2) mode is considerably more dominant for face-on events.

3. Events with $q = 8$

The trends for the $M = 10^6 M_\odot$, $q = 8$ events are largely the same as the trends for $q = 4$ and the same total mass, only the biases are noticeably more pronounced, especially at larger inclination angles. This is consistent with what we expect: the higher mode content is generally more significant for more asymmetric binaries.

As with the $q = 4$ and $q = 1.1$ events, we see that the 1-mode template performs better than the 2, 3, and 4 mode templates in the $\iota = \pi/12$ case.

C. MBHBs with $M = 3 \times 10^5 M_\odot$

Noting the stark difference between biases for the $10^5 M_\odot$ and $10^6 M_\odot$ total mass binaries, we performed PE on a few events with intermediate masses to see if we could determine when biases begin to appear. The PE results for events with total mass $M = 3 \times 10^5 M_\odot$ are shown in Fig. 9. We performed all of the intermediate-mass PE runs at $\iota = \pi/3$.

We first note that the general behavior is as we expect: the posteriors are tighter (looser) and biases are worse (better) than they were with the $10^5 M_\odot$ ($10^6 M_\odot$) events. Moreover, the performance with different mode configurations is quite consistent with what we expect: the 1-mode template performs worst, then the 2-mode template, then

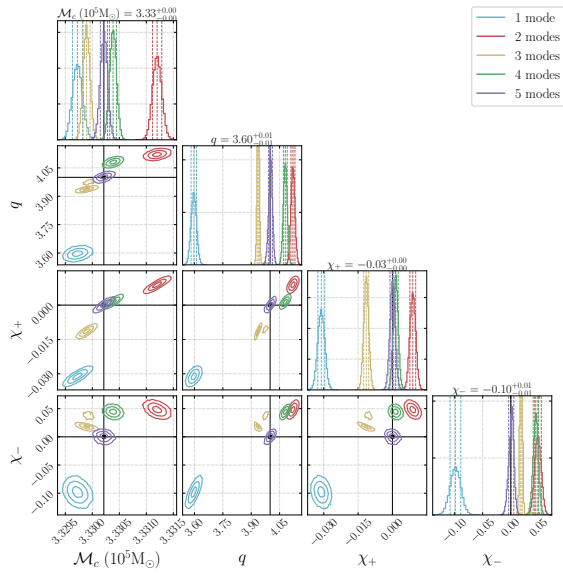
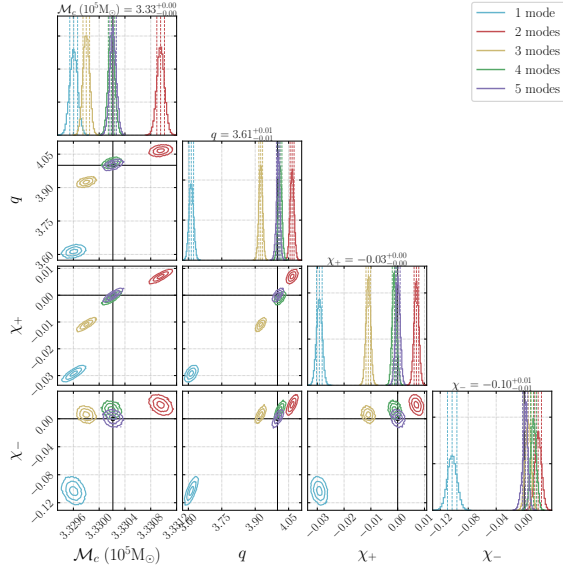
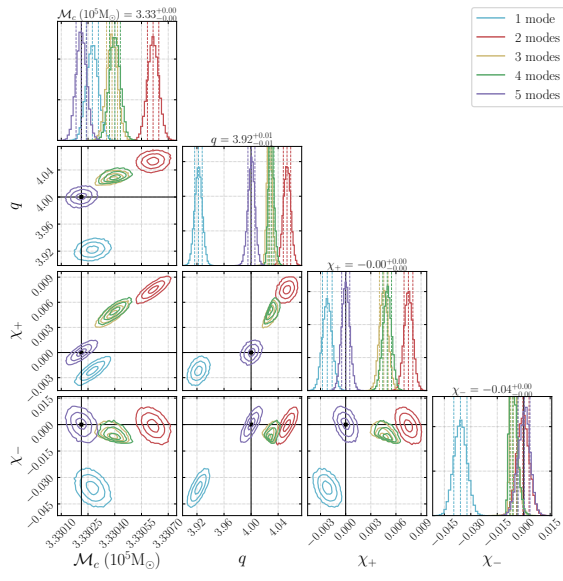


FIG. 7. $M = 10^6 M_\odot$, $q = 4$, $\iota = [\pi/12, \pi/3, \pi/2 - \pi/12]$, total SNR = [2777.1, 1658.0, 1228.5].

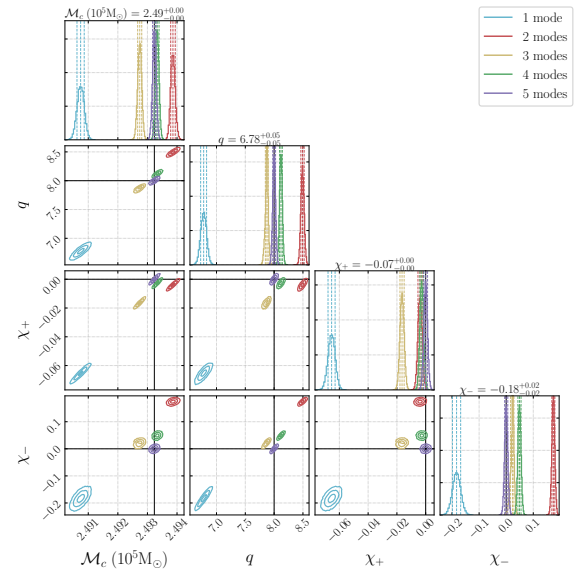
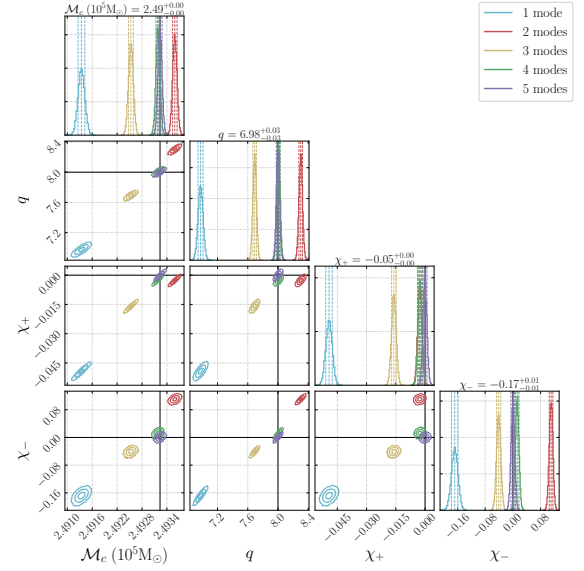
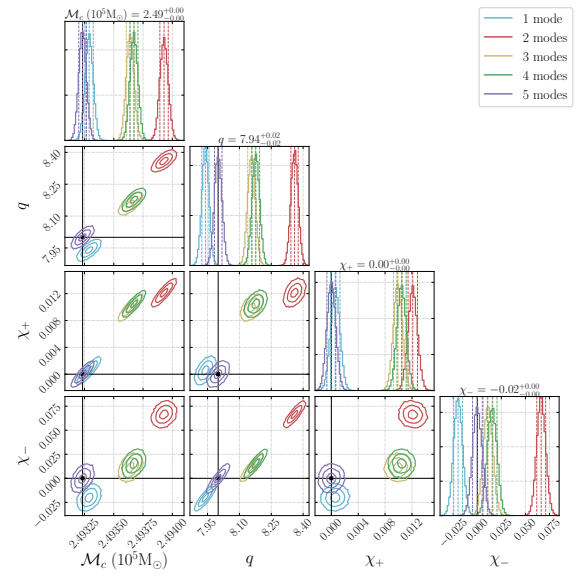


FIG. 8. $M = 10^6 M_\odot$, $q = 8$, $\iota = [\pi/12, \pi/3, \pi/2 - \pi/12]$, total SNR = [1876.8, 1161.1, 873.1].

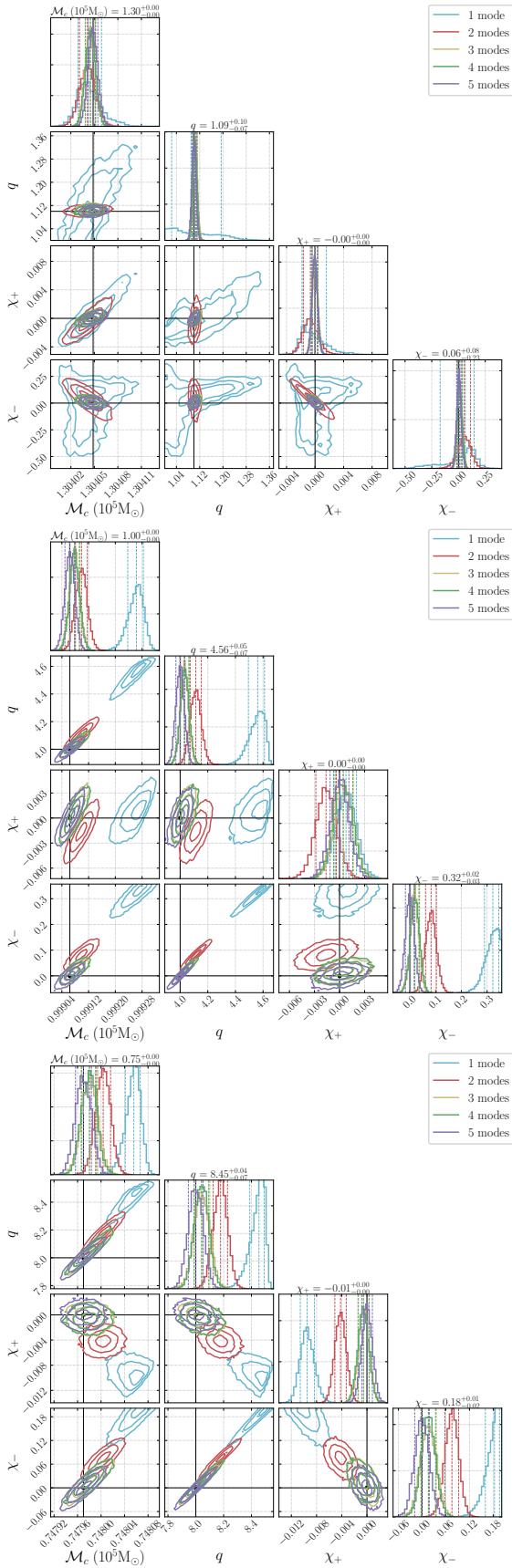


FIG. 9. $M = 3 \times 10^5 M_\odot$, $\iota = \pi/3$, $q = [1.1, 4, 8]$, total SNR = [932.4, 729.5, 563.2].

3-mode, then 4-mode, and then (as always) we recover the injected signal with all 5 modes. We note that the posteriors with one mode are quite broad in the $q = 1.1$ case, similar to what we found for the nearly symmetric binaries with $M = 10^5 M_\odot$. The performance for the $q = 4$ and $q = 8$ events are quite similar.

IV. BIASES INTRODUCED IN EXTRINSIC PARAMETER RECOVERY

We now observe how changing the mode content of the templates affects the recovered posteriors on the extrinsic parameters. The sky localization of events detected by LISA will be crucial for performing follow-up electromagnetic observations of MBHB systems. Previous studies have shown that LISA’s inference of a system’s sky position can be multimodal, and is strongly informed by higher harmonics, particularly at high masses [41]. As a consequence, mismodelling the higher-modes content of the signal can be expected to lead to biases. This contrasts with LVK observations, where most of the information about the sky position comes from triangulating the time of arrival in different detectors, which is mostly independent of the physical content of the waveforms. We attempt to understand how biases can change with differing waveform mode content.

A few representative corner plots illustrating our inference of extrinsic parameters are given in Fig. 10. Below, we highlight a few patterns that we observe:

1. The extrinsic parameters for all the $10^5 M_\odot$ events with either $\iota = \pi/3$ or $\iota \approx \pi/2$ are recovered with very little bias for all mode configurations, and only degenerate in φ and ψ_L for the quadrupole-only templates, as expected. An example is given in the top left panel of Fig. 10 ($10^5 M_\odot$, $q = 4$, $\iota \approx \pi/2$). The recovery with only the (2, 2) mode is noticeably worse for the nearly face-on events with this total mass (compare top left and right panels of Fig. 10). We have observed that, for a nearly face-on, equal-mass system with this lower total mass, higher-order modes become barely distinguishable, so that adding them to the waveform template does not change the PE significantly (but we do not show the corresponding plot for brevity).
2. As for the intrinsic parameters, the biases in extrinsic parameter posteriors become severe for the $10^6 M_\odot$ binaries (example shown in bottom left panel of Fig. 10), with injected values generally only being correctly recovered when all five modes are included in the template. Notably, however, adding just the (3, 3) mode still breaks the degeneracies in φ and ψ_L that exist in parameter recovery with just the (2, 2) mode (see point 4).
3. As expected, the results for the $3 \times 10^5 M_\odot$ events are somewhere in between cases 1 and 2, with moderate

biases in extrinsic parameter recovery (see bottom right panel of Fig. 10).

4. While the degeneracy along constant lines of $\varphi + \psi_L$ and $\varphi - \psi_L$ noted in Ref. [41] is evident in nearly all posteriors obtained with (2, 2)-mode only templates, this degeneracy is consistently lifted with the inclusion of even just one subdominant mode. This can be seen in any of the four panels of Fig. 10.
5. The constraints on the source localization, i.e., the LISA-frame ecliptic longitude and latitude (λ_L, β_L) (among other parameters), improve drastically with the inclusion of one additional mode beyond the (2, 2). This behavior is also noted in Ref. [41].
6. Similarly, the distance-inclination degeneracy commonly observed with quadrupole-only templates is broken by the presence of even one additional mode. This is expected, given the different dependence of the different angular harmonics on the inclination angle.

V. UNDERSTANDING SYSTEMATIC BIASES WITHOUT FULL PARAMETER ESTIMATION

We now turn our attention to using the CV and direct likelihood optimization approaches introduced in Secs. II B and II C to quickly and cheaply estimate the sorts of biases observed in Secs. III and IV. In Sec. V A, we discuss how well the two methods predict the biases seen in PE. In Sec. V B, we estimate the boundaries on parameter space where unbiased PE is possible using the direct likelihood optimization technique.

A. Comparison of cheap methods with parameter estimation

We begin by showing how well the CV and direct likelihood optimization approaches are able to recover the systematic biases observed in PE.

In Fig. 11, we plot the biases on intrinsic MBHB parameters as estimated in the CV approximation (red squares), with the direct likelihood optimization method (navy crosses), and as recovered in our PE runs (green violin plots, with 5% and 95% quantiles marked by the green lines). Each panel shows results for a single MBHB parameter, with five different plots per panel corresponding to different numbers of modes in the waveform template as indicated on the x -axis. In this figure, we show results for one of the events with significant systematic biases ($M = 10^6 M_\odot, q = 8, \iota = \pi/12$).

Both the CV and direct likelihood optimization methods recover the biases in PE fairly well in Fig. 11, with direct likelihood optimization sometimes recovering the center of the posteriors from PE with slightly better accuracy. Both methods likewise perform fairly well in

recovering biases on the extrinsic parameters of this event (again, with direct likelihood optimization performing slightly better), except in the (2, 2)-mode-only case. We show this case in Fig. 12, where we plainly see that direct likelihood optimization performs better than the CV approach. The rest of the extrinsic parameter results for this event are given in Appendix C.

We find this superior performance of the direct likelihood optimization method in cases of severe bias to generally be true, particularly for nearly equal-mass events. To illustrate this further, in Fig. 13 we plot the biases on extrinsic parameters for the $M = 10^6 M_\odot, \iota = \pi/3, q = 1.1$ event. Here, it is evident that the biases are recovered much more accurately when we directly maximize the likelihood than when we use the linear signal approximation. This is also true for the intrinsic parameters (not shown), although the CV performance is not quite as bad.

Notably, calculating the bias with direct likelihood optimization for the events shown in Fig. 11 and Fig. 13 took 11 seconds and 34 seconds, respectively, when running in a Jupyter Notebook on a single core. The results we show in these figures were obtained starting with an initial simplex with parameters set 20σ away from their injected values, and when iterating the procedure 3 and 15 times, respectively. For all but one of the $M = 10^6 M_\odot$ events, we found that with an initial simplex of this size (20σ), 15 iterations were generally more than enough to converge to similarly accurate estimations of the biases as the ones shown in Figs. 11–13. For some events (e.g., the $q = 4, \iota = \pi/3$ and the $q = 8, \iota = \pi/3$ events), no iteration of the Nelder-Mead optimization algorithm was necessary; that is, running the algorithm only once was sufficient to find a maximum likelihood that agreed with PE. In such cases, the estimated bias calculations take as little as 9 seconds.

As mentioned previously, there is one case in which neither the CV approach nor the direct likelihood optimization is able to predict the systematic biases very well, and that is for the event with $M = 10^6 M_\odot, q = 1.1, \iota = \pi/12$. We note that this is the case for which the quadrupole is so dominant that interpreting the effect of adding higher-order modes is not straightforward.

Before concluding this section, we note that the CV approach requires us to be able to take derivatives of the waveform with respect to the parameters: see Eqs. (B9) and (B10). As mentioned before, there are sometimes stability issues in differentiating the (3, 2) mode in the IMRPHEMOMXHM family, so including this mode in CV estimates would require careful monitoring of the differentiation at each step. For this reason, the direct likelihood optimization via Nelder-Mead (which performs gradient-free minimization) has another advantage compared to the CV approach.

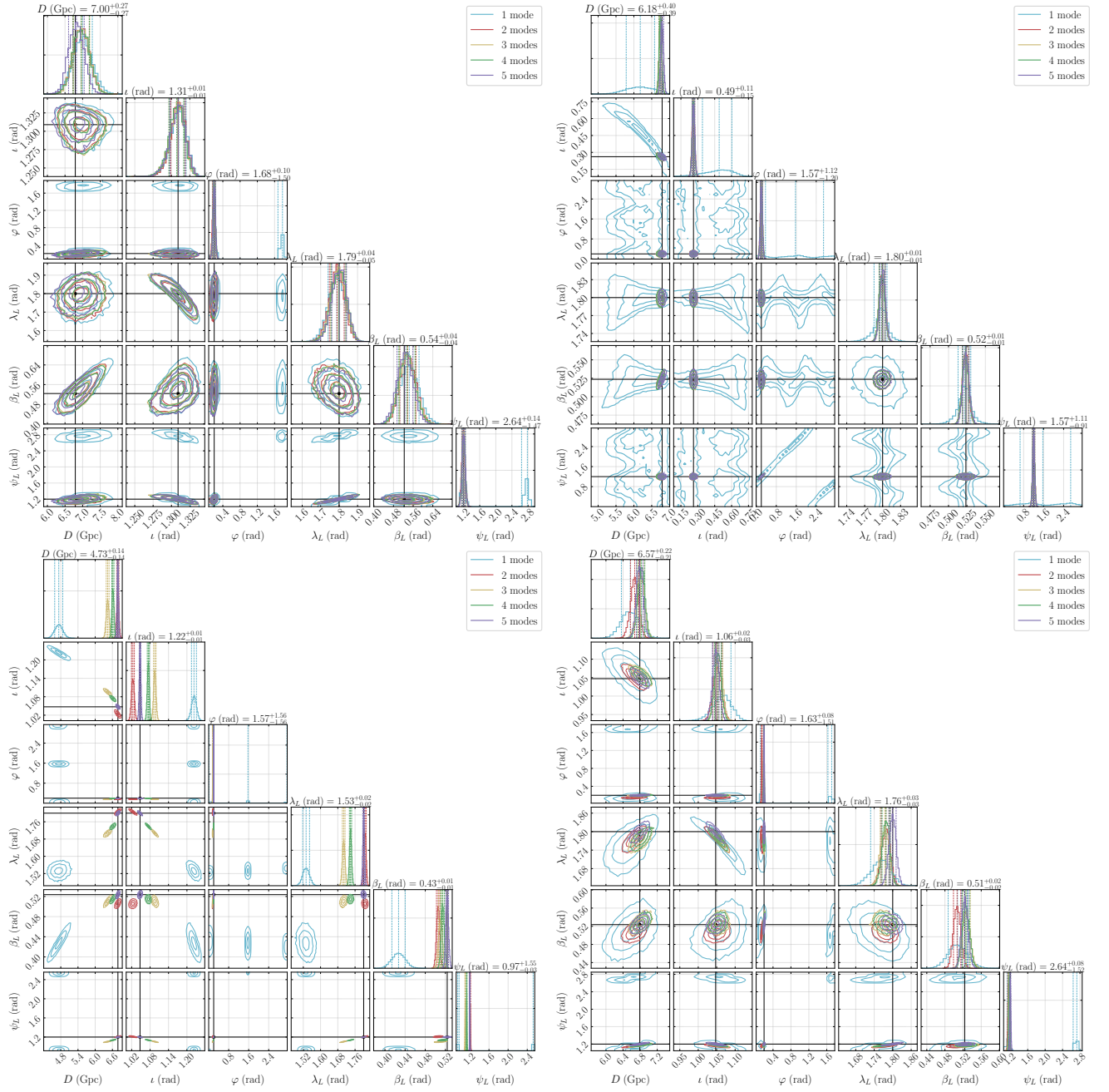


FIG. 10. Extrinsic parameter recovery for selected events. Top left: $M = 10^5 M_\odot, \iota = \pi/2 - \pi/12, q = 4$. Top right: $M = 10^5 M_\odot, \iota = \pi/12, q = 4$. Bottom left: $M = 10^6 M_\odot, \iota = \pi/3, q = 8$. Bottom right: $M = 3 \times 10^5 M_\odot, \iota = \pi/3, q = 8$.

B. Using direct likelihood optimization to set boundaries on unbiased parameter space

Having determined that directly optimizing the likelihood is the better method of cheaply estimating systematic biases due to neglecting higher-order modes, we proceeded to make the heatmap shown in the introduction (Fig. 1) using this method. For each point of fixed total mass and mass ratio, we compute the systematic biases, $\Delta_{\text{sys}}\theta^i$, using the direct likelihood optimization

method. To account for the fact that the optimization algorithm occasionally fails, we draw a random redshift value from $z_{\text{opt}} \in [1, 10]$ until a redshift is found at which 15 steps of the optimization algorithm can be successfully completed. (Note: 15 steps were generally completed with the very first random redshift that was drawn, consistent with the good performance of optimization via the Nelder-Mead algorithm discussed in Sec. II C). We stress that there is nothing physically significant about randomly drawing redshift values here; it is merely a

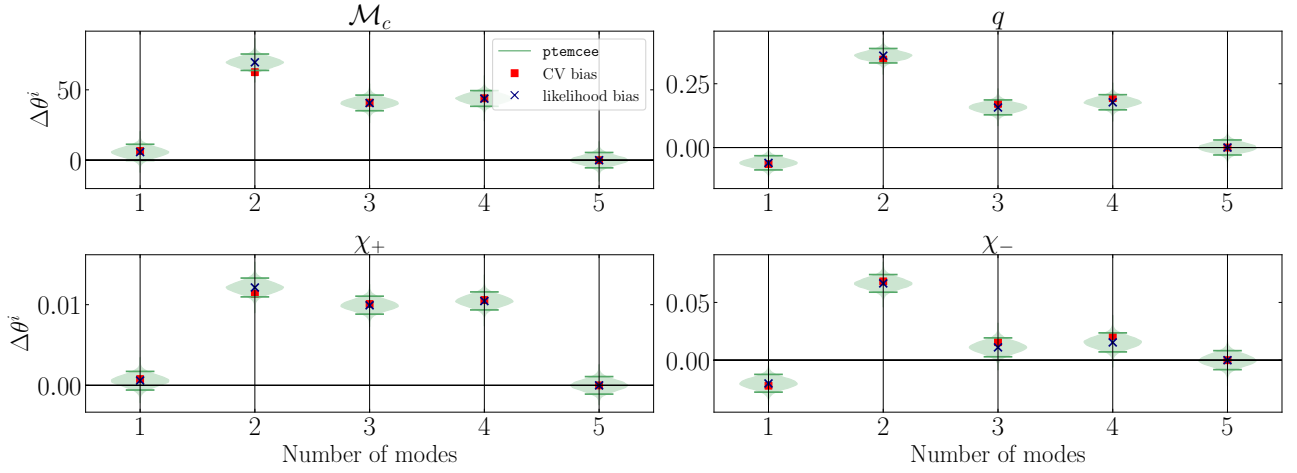


FIG. 11. Systematic bias on intrinsic parameters estimated within the linear signal approximation (“CV bias”) and with the direct likelihood optimization method (“likelihood bias”) compared to biases recovered in full PE (“ptmcee”). Results are shown for the $M = 10^6 M_\odot$, $q = 8$, $\iota = \pi/12$ event. For this event, both “cheaper” methods are able to recover the biases in PE for intrinsic parameters, with direct likelihood optimization performing slightly better.

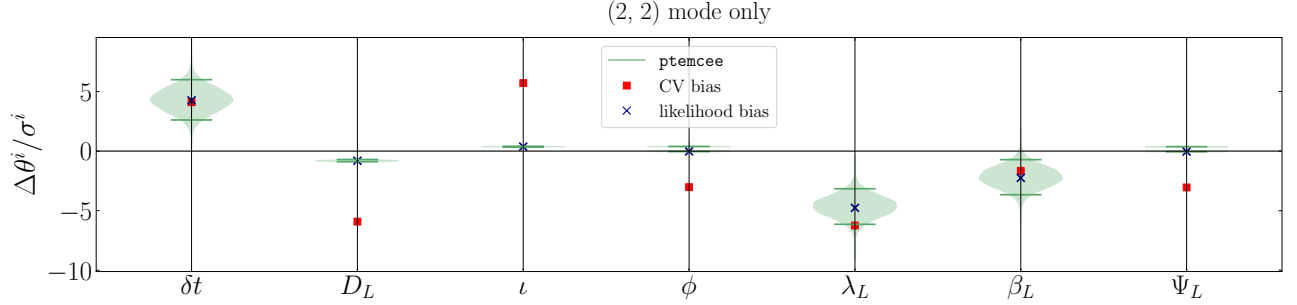


FIG. 12. Biases on extrinsic parameters for the same $M = 10^6 M_\odot$, $q = 8$, $\iota = \pi/12$ event shown in Fig. 11, as recovered with the (2, 2)-mode-only template. Note that for visualization purposes, we plot $\Delta\theta^i / \sigma^i$ in this figure, as opposed to $\Delta\theta^i$ as in Fig. 11.

convenient way to initialize the optimization process multiple times when necessary, that is, in case it occasionally fails. We find that there are some regions (in particular, around $4 \leq q \leq 7$) in which the optimization algorithm seems more sensitive to initial conditions. To mitigate this effect, we continue looking for values of z_{opt} at which the optimization is successfully completed until we find multiple initializations (values of z_{opt}) which return the same values for the systematic biases. We then take such a systematic bias estimation to be “good”.

We next compute the minimum redshift at which our PE is unbiased, i.e., where

$$\Delta_{\text{sys}}\theta^i \leq 2\sigma^i, \quad (2)$$

with the statistical error on the i^{th} parameter, $2\sigma^i$, computed via the Fisher information matrix. To find the redshift at which this occurs, we leverage the simple scaling of errors computed via Fisher analysis, i.e.,

$$\frac{\sigma^i(z_{\text{opt}})}{\sigma^i(z)} = \frac{D_L(z_{\text{opt}})}{D_L(z)}. \quad (3)$$

This relation holds for statistical errors on all parameters except $\theta^i = D_L$, in which case the right-hand side of Eq. (3) is squared. (On the other hand, the systematic bias on D_L also scales with the distance, unlike the systematic biases on all other parameters. The final expression for minimum distance in Eq. (4) therefore also ultimately holds for the bias on luminosity distance as well.) The luminosity distance at which we have unbiased parameter inference is then

$$D_L(z) = \frac{\Delta_{\text{sys}}\theta^i D_L(z_{\text{opt}})}{2\sigma^i(z_{\text{opt}})}, \quad (4)$$

from which one can get the corresponding redshift. (The minimum redshift we consider is $z = 0.1$; if the redshift determined via Eq. (4) is less than this value, we simply set it to $z = 0.1$.) For the sky localization, we look for the redshift at which

$$\left(\begin{array}{c} \Delta_{\text{sys}}\lambda_L \\ \Delta_{\text{sys}}\beta_L \end{array} \right)^T \Sigma^{-1} \left(\begin{array}{c} \Delta_{\text{sys}}\lambda_L \\ \Delta_{\text{sys}}\beta_L \end{array} \right) \leq \chi_{\text{ppf}}^2(0.95, \text{df} = 2), \quad (5)$$

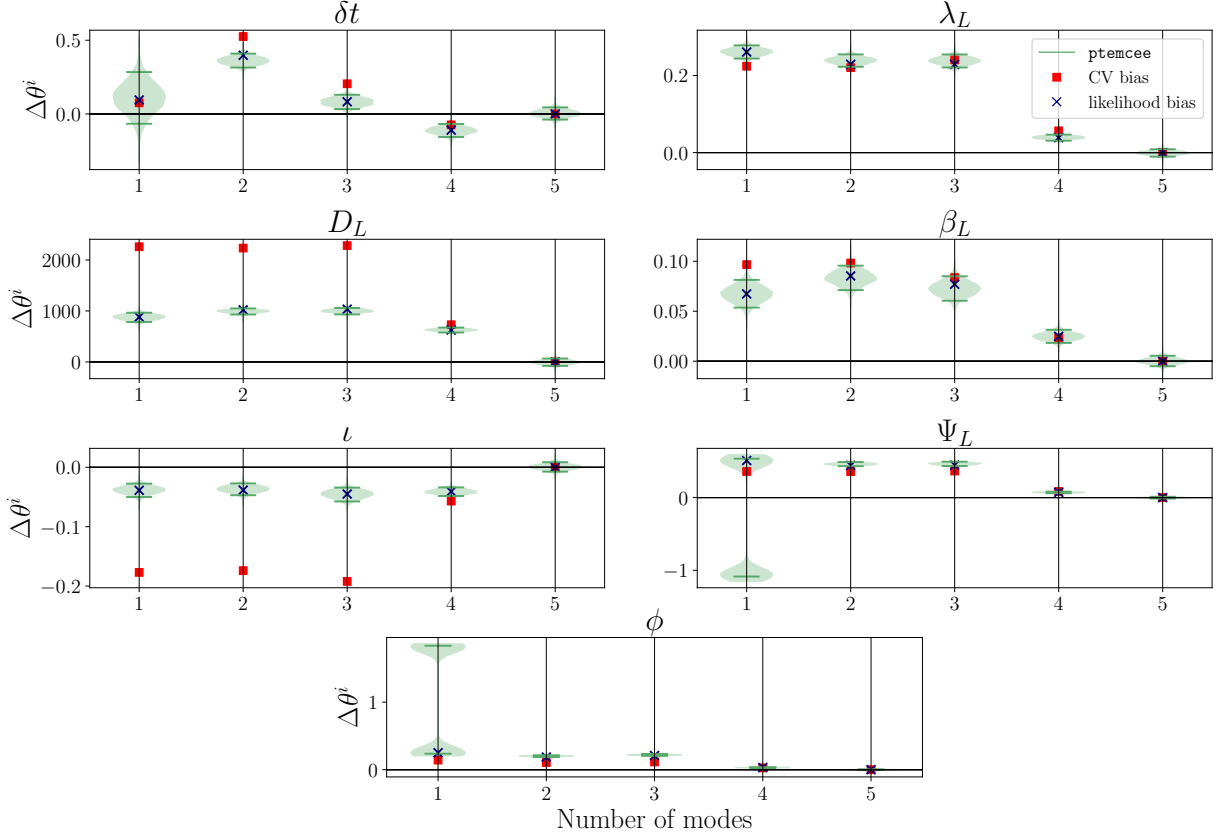


FIG. 13. Biases on extrinsic parameters for the $M = 10^6 M_\odot, \iota = \pi/3, q = 1.1$ event. Direct likelihood optimization performs significantly better than CV in this case.

with Σ the 2×2 covariance matrix between variables λ_L and β_L , and $\chi_{\text{ppf}}^2(0.95, \text{df} = 2)$ the percent-point function for a chi-squared distribution with two degrees of freedom at the 95% confidence level.

The “minimum redshift” calculated in this manner for unbiased PE of the intrinsic parameters is indicated by the color in each bin of Fig. 1. The more blue the square, the less biased the PE is, and the nearer a system can be without finding biases due to excluding the (3, 2) mode.

In Fig. 14, we show the minimum redshift at which the inference of the distance and sky localization is unbiased when neglecting the (3, 2) mode, again for the inclination $\iota = \pi/3$, as in Fig. 1. The presence of two separate regions of larger bias for the sky localization (more pink) can be explained on the one hand by larger signal strength (enhanced for lower q at a fixed total mass, i.e., higher \mathcal{M}_c) and, on the other hand, longer duration of the signal (enhanced for lower \mathcal{M}_c).

In Fig. 15, we show the corresponding plots for when the (3, 2) mode is excluded in PE on nearly edge-on systems ($\iota \approx \pi/2$). While the morphology is about the same as in the plots with $\iota = \pi/3$ for both the intrinsic and extrinsic parameters, we note that the minimum redshift range is noticeably higher for edge-on systems. This is consistent with the observation that higher modes generally become

more significant as the inclination approaches $\pi/2$.

Finally, we comment on the fact that we do not include plots for the nearly face-on events ($\iota = \pi/12$). On the one hand, the quadrupole is quite dominant at this inclination angle, so we already expect higher modes to have a less significant impact. In addition, recalling Fig. 2, we find that at this inclination, it is either the (4, 4) or the (2, 1) that is the quietest mode throughout the parameter space we consider here, rather than the (3, 2). To examine the impact of removing the quietest mode as done in Figs. 1, 14, and 15, we would therefore perform the likelihood optimization excluding one of these modes. However, we found that the likelihood is difficult to optimize when the (3, 2) mode is included, with different initializations of the Nelder-Mead algorithm often giving different final results for the systematic bias. We suspect that mode-mixing for the (3, 2) mode contributes to the instability we find when trying to optimize the likelihood. We note that one can still use the formalism we introduce here to study the effect of removing any other modes, as long as the (3, 2) is also excluded to avoid this stability issue. For example, one could reproduce Fig. 15 with “injected” modes [(2, 2), (3, 3), (2, 1), (4, 4)] and “recover” with modes [(2, 2), (3, 3), (2, 1)] to study the effect of removing the (4, 4) mode.

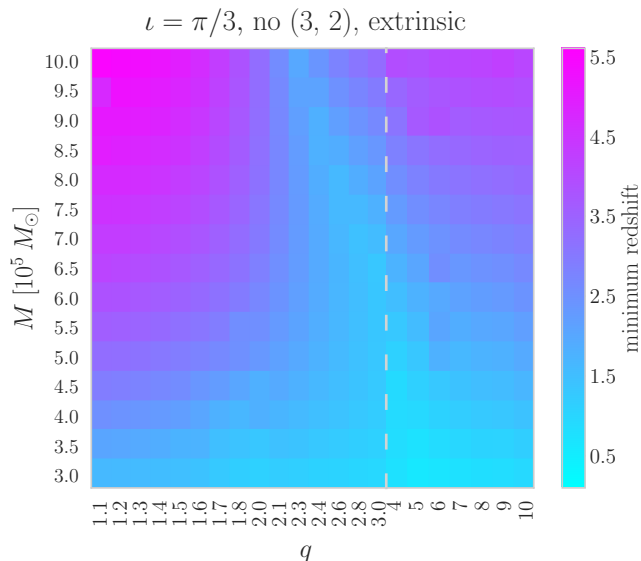


FIG. 14. Minimum redshift at which parameter estimation on the luminosity distance and sky position with $\iota = \pi/3$ is unbiased with the (3, 2) mode excluded from the template for recovery (e.g., parameter estimation is biased for $z \lesssim 3$ for $M = 6 \times 10^5 M_\odot$ and $q = 2$).

VI. EXTRAPOLATING THE MODE CONTENT: APPROXIMATING $\ell \geq 4$ WAVEFORMS

In the above results, we see clearly that parameter recovery for a GW signal with radiation modeled in five modes can be significantly biased even when neglecting only one higher-order mode. Given this result, we cannot assume that the biases cease here; that is, we are not guaranteed that biases will be negligible when injecting a signal with six modes and recovering with five or less, injecting with seven modes and recovering with six or less, etc., particularly when we look at potentially even higher-mass events, (i.e., the “golden” MBHB LISA sources with total mass $\sim 10^7 M_\odot$ or higher [17]), which will have both a larger overall SNR and more merger/ringdown-dominated signals, where higher-order modes become more important. While a thorough investigation of such effects is only possible with waveform templates that accurately model gravitational radiation in higher angular harmonics for a range of BBH configurations, here we show that with rough approximations to such waveforms motivated by PN theory, we can already begin to see the effects of neglecting the modes that are currently absent in waveform approximants.

A. Approximate higher-order mode waveforms from PN theory

1. Approximate amplitudes

To construct rough approximations to higher-order mode amplitudes, we follow the procedure used in Ref. [37] to construct higher-order mode templates for searches of the LVK O3 data. This is essentially the *quadrupole mapping* procedure used to construct the IMRPHENOMHM waveform family [52]. In this procedure, higher-order mode amplitudes are constructed by rescaling the (2, 2) amplitude by the lowest-order PN amplitude terms for each higher multipole. These terms are taken from Sec. 3 of Ref. [53] (with updated versions for $\ell \leq 4$ terms in App. E of Ref. [42]). Explicitly, the expressions for the first five ($\ell = m$) terms are

$$\begin{aligned} H_{22} &\equiv -1 + \left(\frac{323}{224} - \frac{451\eta}{168} \right) V_2^2 + \mathcal{O}(V_2^3), \\ H_{33} &\equiv -\frac{3}{4} \sqrt{\frac{5}{7}} \left(\frac{1-q}{1+q} \right) V_3 + \mathcal{O}(V_3^3), \\ H_{44} &\equiv -\frac{4}{9} \sqrt{\frac{10}{7}} (1-3\eta) V_4^2 + \mathcal{O}(V_4^4), \\ H_{55} &\equiv -\frac{125}{96} \sqrt{\frac{5}{33}} \left(\frac{1-q}{1+q} \right) (1-2\eta) V_5^3 + \mathcal{O}(V_5^5), \\ H_{66} &\equiv -\frac{18}{5} \sqrt{\frac{3}{143}} (1-5\eta+5\eta^2) V_6^4 + \mathcal{O}(V_6^5), \end{aligned} \quad (6)$$

where η is the symmetric mass ratio, $\eta = m_1 m_2 / M^2$ (with $M = m_1 + m_2$), and the V_k are frequency-domain PN parameters given by $V_k(f) = [2\pi M f / k]^{1/3}$. These $H_{\ell m}$ ’s in PN theory are related to the gravitational waveform by the following equations (see Eqs. (9)–(11) of Ref. [53]):

$$\begin{aligned} h(\theta, \phi) &= \sum_{\ell=2}^{+\infty} \sum_{m=-\ell}^{\ell} h_{\ell m} {}_{-2}Y_{\ell m}(\theta, \phi) \\ \tilde{h}_{\ell m} &= \frac{M^2}{D_L} \pi \sqrt{\frac{2\eta}{3}} V_m^{-7/2} e^{-i(m\Psi_{\text{SPA}} + \pi/4)} H_{\ell m}, \end{aligned} \quad (7)$$

where Ψ_{SPA} is the phase in the stationary phase approximation, and we have placed the tilde over $h_{\ell m}$ in the second line to emphasize that these are Fourier-domain expressions for the modes. Both Ψ_{SPA} and $H_{\ell m}$ in the second line are functions of V_m .

Given this information, the authors of Ref. [37] then construct effective amplitude equations for higher-order modes, given the full waveform for the quadrupole, by dividing both the angular dependence and the $H_{\ell m}$ ’s of each higher-order mode by that of the quadrupole, i.e.,

$$\begin{aligned} \left| \frac{h_{33}(3f)}{h_{22}(2f)} \right| &\simeq \frac{3\sqrt{3}}{4\sqrt{2}} \left(\frac{1-q}{1+q} \right) (2\pi M f)^{1/3} \sin(\iota), \\ \left| \frac{h_{44}(4f)}{h_{22}(2f)} \right| &\simeq \frac{2\sqrt{2}}{3} (1-3\eta) (2\pi M f)^{2/3} \sin^2(\iota), \end{aligned} \quad (9)$$

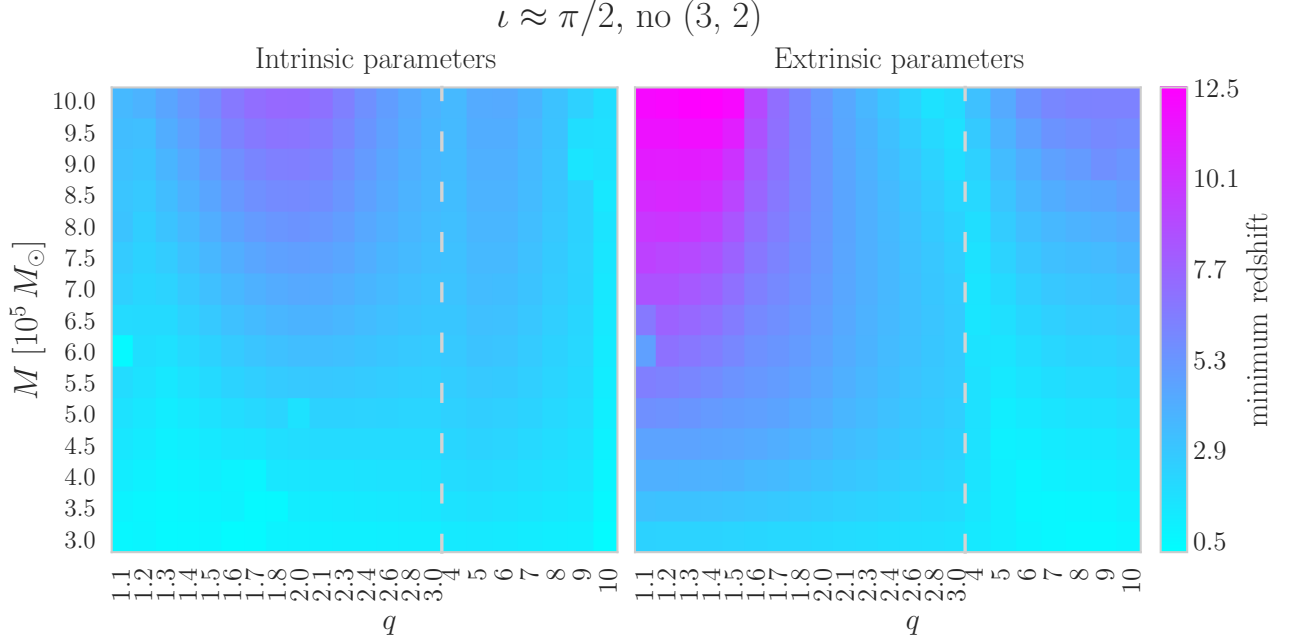


FIG. 15. Same as Fig. 14 but for nearly-edge-on systems. We plot the minimum redshift for unbiased parameter recovery without the (3, 2) mode. Plots are shown for parameters $[M_c, q, \chi_+, \chi_-]$ on the left, and for the sky localization and distance on the right.

$$\left| \frac{h_{55}(5f)}{h_{22}(2f)} \right| \simeq \frac{125}{192} \sqrt{\frac{5}{2}} \left(\frac{1-q}{1+q} \right) (1-2\eta)(2\pi Mf) \sin^3(\iota),$$

$$\left| \frac{h_{66}(6f)}{h_{22}(2f)} \right| \simeq \frac{27\sqrt{3}}{40} (1-5\eta+5\eta^2)(2\pi Mf)^{4/3} \sin^4(\iota).$$

Note that compared to Eq. (11) of Ref. [37], we have the additional expressions for $\ell = m = 5$ and $\ell = m = 6$.

In this work, we are interested in reconstructing modes with $\ell \geq 5$, at variance with Ref. [37], which focused on building only the (3, 3) and (4, 4) modes from the quadrupole. In this case, it is interesting to ask whether more accurate higher-order mode waveforms can be built by approximating $\ell \geq 5$ modes from the (3, 3) or (4, 4) modes, rather than the quadrupole. To investigate this, we additionally compute the following terms:

$$\left| \frac{h_{44}(4f)}{h_{33}(3f)} \right| \simeq \frac{16}{9\sqrt{3}} \left(\frac{1+q}{1-q} \right) (1-3\eta)(2\pi Mf)^{1/3} \sin(\iota) \quad (10)$$

$$\left| \frac{h_{55}(5f)}{h_{44}(4f)} \right| \simeq \frac{125\sqrt{5}}{256} \left(\frac{1-q}{1+q} \right) \frac{(1-2\eta)}{(1-3\eta)} (2\pi Mf)^{1/3} \sin(\iota),$$

$$\left| \frac{h_{66}(6f)}{h_{44}(4f)} \right| \simeq \frac{81}{80} \sqrt{\frac{3}{2}} \frac{(1-5\eta+5\eta^2)}{1-3\eta} (2\pi Mf)^{2/3} \sin^2(\iota).$$

In the top panel of Fig. 16, we plot the approximate amplitudes we obtained for h_{55} and h_{66} , rescaling from both the (2, 2) (dashed lines) and (4, 4) (dot-dashed lines) waveforms. The system plotted in Fig. 16 has total mass and mass ratio $M = 10^6 M_\odot$ and $q = 8$. For comparison, we show in the bottom panel how the approximate (3, 3) and (4, 4) amplitude expressions rescaled from the

quadrupole (dashed lines) compare to the “exact” IMRPHENOMXHM amplitudes (solid lines). This bottom panel is essentially a reproduction of Fig. 6 of Ref. [37], but for a much heavier BBH system. Compared to the top panel of Fig. 6 of Ref. [37], we also show an approximate (4, 4) waveform that is rescaled from the (3, 3) IMRPHENOMXHM waveform (dotted yellow line).

2. Approximate phases

To approximate the phases of higher-order modes, we begin by taking

$$\Psi_{\ell m} \approx \frac{m}{2} \Psi_{22} \left(\frac{2f}{m} \right) + \Delta_{\ell m} + \left(1 - \frac{m}{2} \right) \frac{\pi}{4}, \quad (11)$$

with $\Delta_{\ell m}$ the inspiral-portion phase shift given in Eq. (7) of [52],

$$\Delta_{\ell m} = \frac{\pi}{2} [3\ell + \text{mod}(\ell + m, 2)] - \pi. \quad (12)$$

In Fig. 17, we plot the difference between the approximate phases computed via Eq. (11) and the “exact” phases from the IMRPHENOMXHM waveform for the same $M = 10^6 M_\odot$, $q = 8$ system with amplitudes shown in Fig. 16. The approximate phases perform quite well at low frequencies and begin to veer off around the merger. We show the location of the merger frequency (i.e., the point at which the IMRPHENOMXHM (3, 3) and (4, 4) amplitudes are at their maximum) with dotted lines.

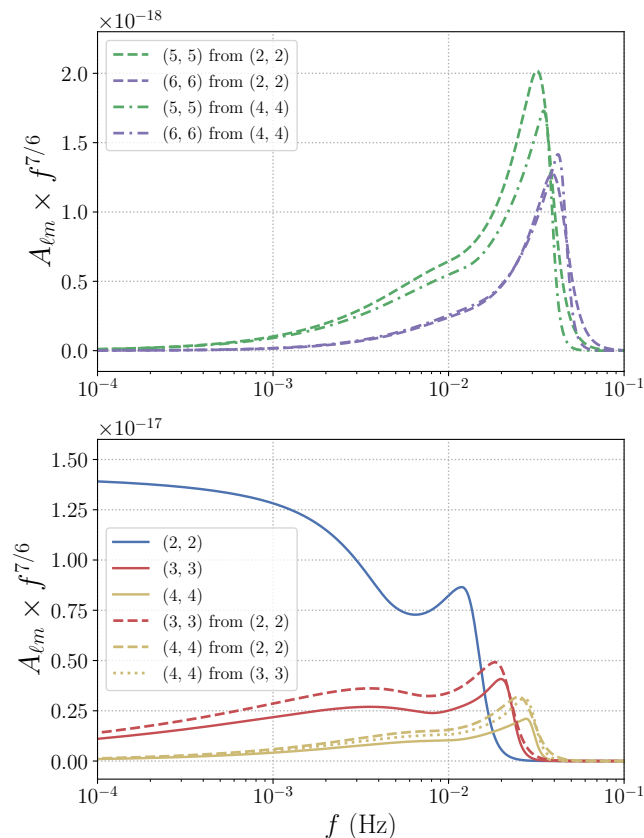


FIG. 16. Neglecting higher-order modes ($\ell \geq 5$) which are not currently modeled within the IMRPHENOMXHM approximant could introduce biases in PE. We therefore approximately model these modes as shown here, and then test them in a PE run in Fig. 18. Top: We model the (5, 5) and (6, 6) modes by rescaling the IMRPHENOMXHM modes for (2, 2) and (4, 4) using the PN-motivated relations in Eqs. (10) and (11). Bottom: As a test of our rescaling method, we show that modeling (3, 3) and (4, 4) using just the (2, 2) IMRPHENOMXHM waveform gives fairly accurate results. All mode amplitudes are plotted for an event with $M = 10^6 M_\odot$, $q = 8$. Dashed, dotted and dot-dashed lines correspond to approximate amplitudes obtained by rescaling the “exact” amplitudes for the (2, 2), (3, 3), and (4, 4) modes, respectively.

As done for the amplitudes, we additionally observed whether higher-order phases might be better approximated from the (3, 3) or (4, 4) modes than the (2, 2), i.e., if we replace $m/2 \times \Psi_{22}(2f/m)$ in Eq. (11) with $m/3 \times \Psi_{33}(3f/m)$ or $m/4 \times \Psi_{44}(4f/m)$. While we sometimes found that approximating from the (3, 3) resulted in a smaller difference from the “exact” phase and/or a more stable phase through merger, we only examined these phenomena for a handful of systems. For the present study, we build the phases simply following Eq. (11), and we leave a more thorough investigation of optimal ways to approximate higher-order modes for future study.

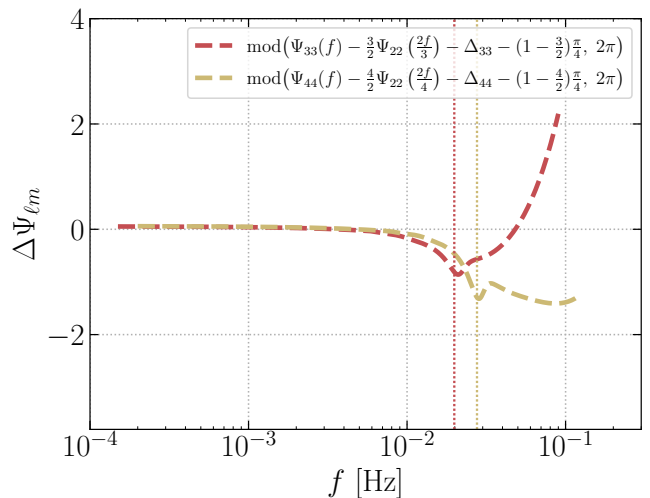


FIG. 17. Similar to the lower panel of Fig. 16, but comparing our approximate PN-based model for the phases of higher modes (see Eq. (11)) instead of amplitudes. We see that our model is fairly accurate at low frequencies. The accuracy begins to degrade slightly as we approach the merger frequencies, shown with dotted lines for each mode. The difference between our approximate phases and the “exact” phases from the IMRPHENOMXHM approximant is shown for the same event with amplitudes given in Fig. 16.

B. Biases with approximate waveforms

We now observe whether we can see noticeable systematic biases of the same sort seen in Secs. III and IV, when we inject a signal with the (5, 5) and (6, 6) modes as modeled with the expressions in Eqs. (10)–(11) and recover with these $\ell \geq 5$ modes removed. The results of such an injection and recovery for the $M = 10^6 M_\odot$, $q = 8$, $\iota \approx \pi/2$ event are shown in Fig. 18.

When injecting the signal with the extrapolated (5, 5) and (6, 6) modes and recovering without the (6, 6) (yellow contours and histograms), the bias is barely discernible. This is fairly unsurprising, given the low relative SNR of the (6, 6) mode ($\text{SNR}_{66}=15.6$, compared to $\text{SNR}_{55}=56$ and $\text{SNR}_{22}=780$). When injecting with both extrapolated modes and recovering without either of them (purple contours and histograms), there are some biases. The recovered values of the intrinsic parameters are near enough to injected values that the bias is unlikely to make a significant difference. However, we note that a few extrinsic parameters, such as the ecliptic longitude and inclination, exhibit biases that could make some difference in the interpretation of the physical system.

In short, our results suggest that while the (5, 5) mode may increase slightly the accuracy of parameter inference of MBHBs, the (6, 6) mode is likely to make a much smaller impact. In addition to the difference in relative SNR of these higher-order modes, we note that in PN theory, even- m modes are generally easier to reconstruct from other modes as compared to odd- m modes. It is

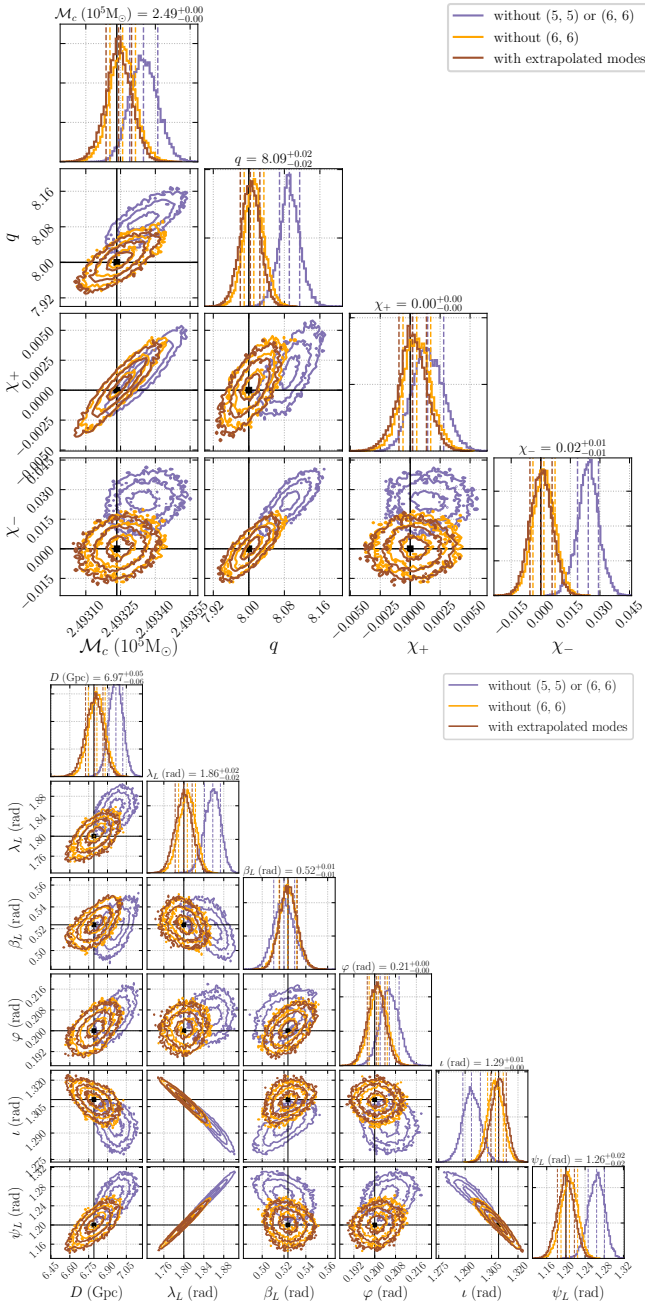


FIG. 18. Parameter recovery with and without the extrapolated (5, 5) and (6, 6) modes (see Figs. 16 and 17). While virtually no bias is seen when excluding just the (6, 6) mode, there is a slight bias when excluding in addition the (5, 5) mode in the template for recovery. For reference, the extrapolated modes have $\text{SNR}_{66}=15.6$ and $\text{SNR}_{55}=56$, compared to $\text{SNR}_{22}=780$.

possible that when the $\ell \geq 5$ modes are removed, the remaining waveform has an easier time reproducing the (6, 6) than the (5, 5) mode, contributing to the lesser bias observed for this mode.

Finally, we note that the system we show these results for is one with some of the most “biased” results (high

total mass and mass ratio, nearly edge-on). We aim to do a future study to determine the relative impact of (5, 5), (6, 6) and higher ℓ modes after marginalizing over inclination (for LISA and also for current and future ground based detectors) [54]. It is worth noting that we expect LISA to detect systems more massive than the ones we considered ($M > 10^6 M_\odot$), and we could also include such systems in our future study. Finally, the biases could be more pronounced for systems with spinning progenitor BHs, a consideration we do not address here.

VII. CONCLUSIONS

We have assessed how the exclusion of higher-order modes would bias our inference of MBHB signals detected with LISA. We find that for events with masses starting at a few times $10^5 M_\odot$, excluding even just the (3, 2) mode can result in significantly biased inference of both intrinsic and extrinsic parameters. We demonstrate how such bias depends on the total mass, mass ratio, and inclination angle of the event by running PE on a coarse grid spanning these parameters. We then fill in this grid with substantially more data points using the direct likelihood optimization method, which we found produces good estimates of the systematic biases due to excluding higher-order modes. The result is an approximate boundary around a region of unbiased PE in the parameter space of total mass, mass ratio, and redshift for a few different inclination angles. We then began to explore how the same effects might persist for the exclusion of higher modes that are not yet modeled with current waveform approximants, using our own crude waveforms motivated by PN theory to begin to answer this question.

There are many avenues for future work. In the first place, it will eventually be important to understand how these biases would appear for binaries with spinning progenitors, including precessing systems. In fact, we expect higher-order modes to be more important for systems with high aligned spins (see, e.g., [26]). Similarly, we will eventually have to account for eccentric systems, systems with even higher mass ratios than what we have explored thus far ($q > 10$), etc.

To carry out some of the above work, it could be useful to further develop some of the tools implemented here. For instance, there is certainly room to improve on the direct likelihood optimization method. One could explore any number of alternative optimization algorithms and see whether they perform better than the Nelder-Mead algorithm for these particular high-dimensional GW problems. Even keeping the Nelder-Mead algorithm, one could perform a more extensive study of how the results depend on the number of iterations, size of the initial simplex, etc.

Moreover, having found potential methods to estimate systematic bias, one could apply the above formalism to investigate systematic biases for BBH sources of ground-based detectors (both current and future). The direct

likelihood optimization method could also be useful in understanding systematic biases due to other waveform inaccuracies, besides the exclusion of higher-order modes (e.g., failing to model precession, eccentricity, etc.).

Finally, much work remains to be done in going beyond the technique we have used in Sec. VI to develop accurate waveforms with higher-order mode content. One could begin by examining in more detail whether rescaling from higher-order modes than the (2, 2) is beneficial across the parameter space. Ultimately, it will be important to answer the question of how many modes are enough to perform unbiased PE on the MBHB sources that will be observed by LISA.

ACKNOWLEDGMENTS

We thank Luca Reali, Veome Kapil, Rohit Chandramouli, Nicolás Yunes, Will Farr, and Leo Stein for helpful discussions. S. Y. is supported by the NSF Graduate Research Fellowship Program under Grant No. DGE2139757. S. Y., F. I., D. W., and E. B. are supported by NSF Grants No. AST-2307146, PHY-2207502, PHY-090003 and PHY-20043, by NASA Grants No. 20-LPS20-0011 and 21-ATP21-0010, by the John Templeton Foundation Grant 62840, by the Simons Foundation, and by the Italian Ministry of Foreign Affairs and International Cooperation grant No. PGR01167. The work of F. I. is supported by a Miller Postdoctoral Fellowship. S. M. acknowledges support from the French space agency CNES in the framework of LISA. This work was carried out at the Advanced Research Computing at Hopkins (ARCH) core facility (rockfish.jhu.edu), which is supported by the NSF Grant No. OAC-1920103.

Appendix A: IMRP_{PHENOM}XHM vs. IMRP_{PHENOM}HM

In this Appendix, we show how the use of different approximants (namely, IMRP_{PHENOM}HM [52] and IMRP_{PHENOM}XHM [42]) affects our PE results. Despite belonging to the same waveform family, these two approximants feature very different procedures to approximate the higher-order mode content of the signal, as we shall see below. Before we proceed, we note that to truly have a direct comparison between results with the different approximants, one would need to carefully align the waveforms in phase, which we do not do here. Our purpose is merely to show qualitatively the effect of using different methods to approximate higher-order modes.

In Fig. 19, we plot posteriors on intrinsic parameters as obtained in PE runs with IMRP_{PHENOM}HM (left column) and IMRP_{PHENOM}XHM (right column). For brevity, in this section we will drop the common “IMRP_{PHENOM}” portion of each approximant name and simply use the labels “XHM” or “HM”. We show the comparisons for both a moderate-bias case ($M = 3 \times 10^5 M_\odot$, top row)

and a case with more severe biases ($M = 10^6 M_\odot$, bottom row).

In the moderate-bias case, the injected values of the intrinsic parameters are recovered fairly accurately with comparatively fewer modes in the template with HM. At first glance, this may be unexpected, since XHM is the newer approximant family (with all modes calibrated to numerical relativity simulations). However, we note that this is not necessarily indicative of HM performing better; on the contrary, it could be that the effect of higher-order modes is underestimated with this approximant, such that including more modes does not accurately capture the full extent of changes in the physical signal. This possibility is supported by the fact that XHM is much better than HM at recovering signals injected with NR surrogate waveforms (see, e.g., Fig. 14 of Ref. [42]).

In the case of severe bias, we see much of the same phenomenon. The mass ratio q and χ_- are recovered considerably worse with HM than XHM when the 1-mode template is used. The recovery of chirp mass and χ_+ with this template is comparable between approximants, but the recovered values of these parameters are again closer to injections with HM than with XHM when using 2, 3, and 4 mode templates. We stress again that this could really be a result of HM underestimating the importance of higher modes for a given system. Extrinsic parameter recovery (not shown) is roughly comparable with either waveform approximant in the cases of both moderate and severe biases.

It is interesting to note that the SNR ordering is generally not the same when determined with the different waveform families. In particular, HM tends to put comparatively more weight in the (4, 4) harmonic, so that the SNR in this harmonic is generally larger than the SNR in the (2, 1) harmonic, whereas the opposite is true for XHM. We note that HM has an additional available mode (the (4, 3) mode) compared to XHM. To make the comparison more straightforward, we compared PE runs between the approximants using only the five modes available with either family.

To summarize, we see that the systematic bias due to insufficient mode content does not appear in the same way when using different waveform approximants (with the former caveat that we are not looking at exactly the same systems, due to the phases not being exactly aligned). Importantly, in the HM family, the higher modes are more simply rescaled from the (2, 2) mode, indeed in much the same manner as we employ in Sec. VI of the main text. In contrast, each mode in the XHM family is calibrated to numerical relativity simulations, such that the modes are in a sense more truly independent from one another. Adding or removing one higher mode can therefore be more consequential with XHM than with HM (i.e., it can alter the waveform more significantly). This sort of phenomenon is important to keep in mind as we move towards more accurate waveform models containing higher-order modes.

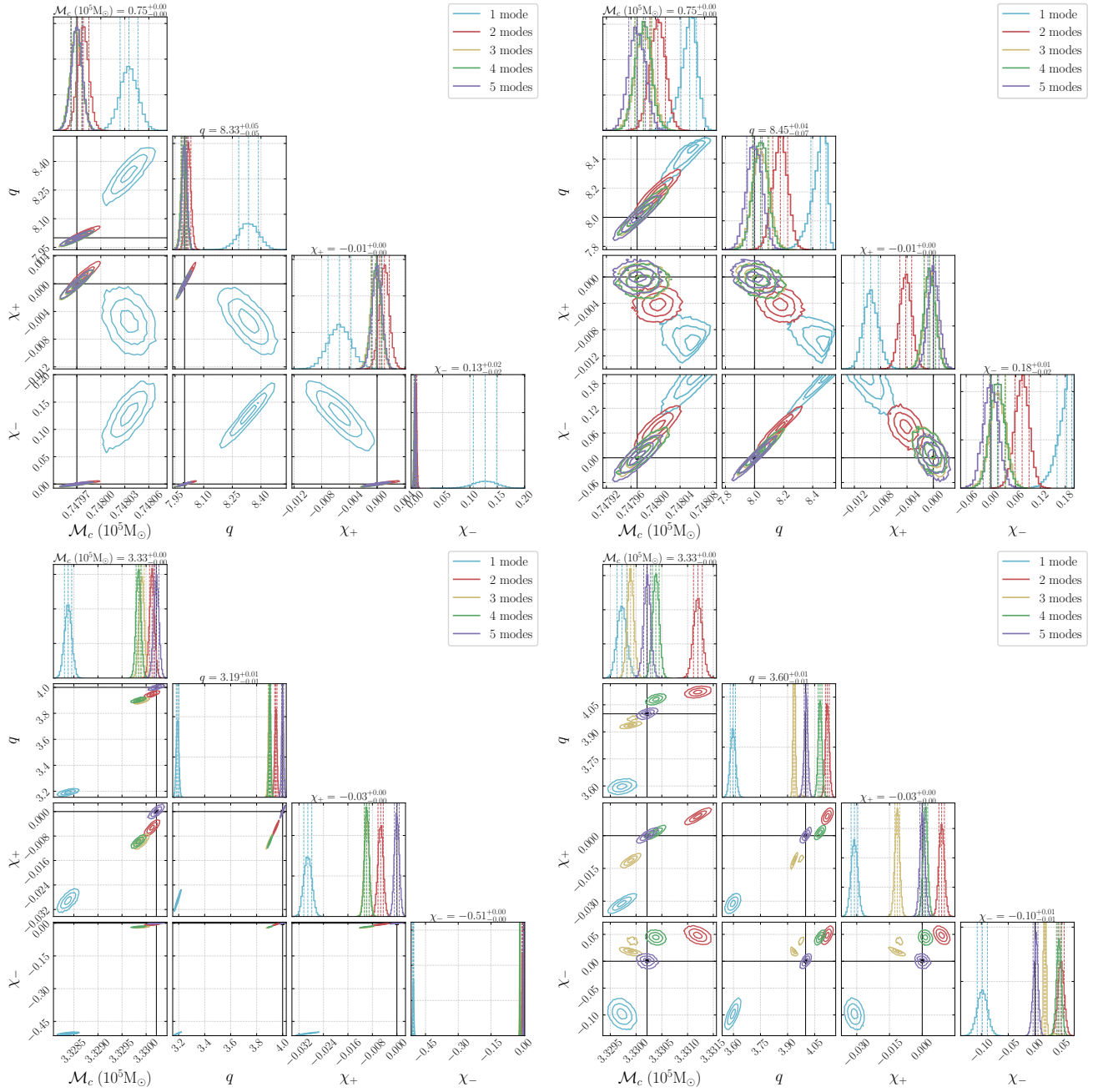


FIG. 19. PE results for a few example systems using the IMRPHENOMHM (left) and IMRPHENOMXHM (right) approximants. Top row: $M = 3 \times 10^5 M_\odot$, $\iota = \pi/3$, $q = 8$. Bottom row: $M = 10^6 M_\odot$, $\iota = \pi/2$, $q = 4$.

Appendix B: Cutler-Vallisneri formalism

In this appendix, we outline for completeness the linear signal approximation introduced by Cutler and Vallisneri [19], which we use as a cheap method to approximate systematic biases due to insufficient mode content in waveform templates.

We write the total signal at a GW detector $s(t)$ as

$$s(t) = h_{\text{GW}}(t) + n(t) \quad (\text{B1})$$

where h_{GW} is the GW signal and $n(t)$ the detector noise, which we take to be stationary and Gaussian. The log likelihood is then given by

$$\ln p(s|\boldsymbol{\theta}) \propto -\frac{1}{2} (s - h_m | s - h_m) \quad (\text{B2})$$

where $\boldsymbol{\theta}$ are the waveform parameters and the approximate waveform template, h_m , will always differ from the true waveform h_{GW} by some amount

$$\delta h(\boldsymbol{\theta}) = h_{\text{GW}}(\boldsymbol{\theta}) - h_m(\boldsymbol{\theta}). \quad (\text{B3})$$

The inner product in Eq. (B2) is given by

$$(a|b) = 4\text{Re} \int_0^\infty \frac{\tilde{a}(f)\tilde{b}^*(f)}{S_n(f)} df, \quad (\text{B4})$$

where the asterisk denotes complex conjugation, $\tilde{a}(f)$ and $\tilde{b}(f)$ are the Fourier transforms of time-domain signals $a(t)$ and $b(t)$, respectively, and $S_n(f)$ is the noise PSD.

The maximum of the likelihood function occurs at some best-fit parameters, $\boldsymbol{\theta}_{\text{bf}}$, such that

$$(\partial_i h_m(\boldsymbol{\theta}_{\text{bf}})|s - h_m(\boldsymbol{\theta}_{\text{bf}})) = 0, \quad (\text{B5})$$

where $\partial_i = \partial/\partial\theta^i$ denotes the partial derivative with respect to parameter θ^i . (The expression in Eq. (B5) can be obtained by demanding that the gradient of the likelihood with respect to θ^i vanishes at $\boldsymbol{\theta} = \boldsymbol{\theta}_{\text{bf}}$.) The linear signal approximation now enters, where for a small perturbation $\boldsymbol{\theta}_{\text{tr}} = \boldsymbol{\theta}_{\text{bf}} + \Delta\boldsymbol{\theta}$, with $\boldsymbol{\theta}_{\text{tr}}$ the true GW parameters, we can expand the waveform near $\boldsymbol{\theta}_{\text{bf}}$ as

$$h_m(\boldsymbol{\theta}_{\text{tr}}) - h_m(\boldsymbol{\theta}_{\text{bf}}) \approx -\Delta\theta^i \partial_i h_m(\boldsymbol{\theta}_{\text{bf}}). \quad (\text{B6})$$

Then we can write the quantity $s - h_m(\boldsymbol{\theta}_{\text{bf}})$ as

$$\begin{aligned} s - h_m(\boldsymbol{\theta}_{\text{bf}}) &= n + h_{\text{GW}}(\boldsymbol{\theta}_{\text{tr}}) \\ &\quad - h_m(\boldsymbol{\theta}_{\text{tr}}) + h_m(\boldsymbol{\theta}_{\text{tr}}) - h_m(\boldsymbol{\theta}_{\text{bf}}) \\ &\approx n + \delta h(\boldsymbol{\theta}_{\text{tr}}) - \Delta\theta^i \partial_i h_m(\boldsymbol{\theta}_{\text{bf}}). \end{aligned} \quad (\text{B7})$$

Equation (B5) then becomes

$$(\partial_i h_m(\boldsymbol{\theta}_{\text{bf}})|s - h_m(\boldsymbol{\theta}_{\text{bf}})) \approx (\partial_i h_m(\boldsymbol{\theta}_{\text{bf}})|n) \quad (\text{B8})$$

$$\begin{aligned} &+ (\partial_i h_m(\boldsymbol{\theta}_{\text{bf}})|\delta h(\boldsymbol{\theta}_{\text{tr}})) \\ &- \Delta\theta^j (\partial_i h_m(\boldsymbol{\theta}_{\text{bf}})|\partial_j h_m(\boldsymbol{\theta}_{\text{bf}})). \end{aligned}$$

Identifying the Fisher matrix Γ_{ij} as

$$\Gamma_{ij} \equiv (\partial_i h_m(\boldsymbol{\theta}_{\text{bf}})|\partial_j h_m(\boldsymbol{\theta}_{\text{bf}})), \quad (\text{B9})$$

we can re-arrange Eq. (B9) to obtain

$$\begin{aligned} \Delta\theta^i &= (\Gamma^{-1}(\boldsymbol{\theta}_{\text{bf}}))^{ij} (\partial_i h_m(\boldsymbol{\theta}_{\text{bf}})|n) \\ &\quad + (\Gamma^{-1}(\boldsymbol{\theta}_{\text{bf}}))^{ij} (\partial_i h_m(\boldsymbol{\theta}_{\text{bf}})|\delta h(\boldsymbol{\theta}_{\text{tr}})). \end{aligned} \quad (\text{B10})$$

The first piece on the right-hand side, $(\Gamma^{-1}(\boldsymbol{\theta}_{\text{bf}}))^{ij} (\partial_i h_m(\boldsymbol{\theta}_{\text{bf}})|n)$, describes errors due to noise and is not the focus of our study here. The second piece, which we will denote $\Delta_{\text{sys}}\theta^i = (\Gamma^{-1}(\boldsymbol{\theta}_{\text{bf}}))^{ij} (\partial_i h_m(\boldsymbol{\theta}_{\text{bf}})|\delta h(\boldsymbol{\theta}_{\text{tr}}))$, is the systematic bias due to imperfect approximation of the true waveform h_{GW} by h_m (due to, in this case, too few harmonics in the template). We calculate $\Delta_{\text{sys}}\theta^i$ for our example events and examine how well this quantity predicts the biases observed in the PE results.

Appendix C: Additional results for the CV and direct likelihood optimization estimates of systematic biases

In Fig. 20, we plot biases as determined by the CV and direct likelihood optimization methods, as well as PE, for the remainder of the extrinsic parameters of the $M = 10^6 M_\odot$, $q = 8$, $\iota = \pi/12$ event discussed in the main text (Figs. 11 and 12).

-
- [1] M. Pürrer and C.-J. Haster, *Phys. Rev. Res.* **2**, 023151 (2020), [arXiv:1912.10055 \[gr-qc\]](#).
- [2] A. Z. Jan, A. B. Yelkar, J. Lange, and R. O’Shaughnessy, *Phys. Rev. D* **102**, 124069 (2020), [arXiv:2011.03571 \[gr-qc\]](#).
- [3] C. J. Moore, E. Finch, R. Busicchio, and D. Gerosa, *iScience* **24**, 102577 (2021), [arXiv:2103.16486 \[gr-qc\]](#).
- [4] Q. Hu and J. Veitch, *Phys. Rev. D* **106**, 044042 (2022), [arXiv:2205.08448 \[gr-qc\]](#).
- [5] Q. Hu and J. Veitch, *Astrophys. J.* **945**, 103 (2023), [arXiv:2210.04769 \[gr-qc\]](#).
- [6] J. S. Read, *Class. Quant. Grav.* **40**, 135002 (2023), [arXiv:2301.06630 \[gr-qc\]](#).
- [7] C. B. Owen, C.-J. Haster, S. Perkins, N. J. Cornish, and N. Yunes, *Phys. Rev. D* **108**, 044018 (2023), [arXiv:2301.11941 \[gr-qc\]](#).
- [8] A. Puecher, A. Samajdar, G. Ashton, C. Van Den Broeck, and T. Dietrich, *Phys. Rev. D* **109**, 023019 (2024), [arXiv:2310.03555 \[gr-qc\]](#).
- [9] A. Jan, D. Ferguson, J. Lange, D. Shoemaker, and A. Zimmerman, *Phys. Rev. D* **110**, 024023 (2024), [arXiv:2312.10241 \[gr-qc\]](#).
- [10] V. Kapil, L. Reali, R. Cotesta, and E. Berti, *Phys. Rev. D* **109**, 104043 (2024), [arXiv:2404.00090 \[gr-qc\]](#).
- [11] A. Dhani, S. Völkel, A. Buonanno, H. Estelles, J. Gair, H. P. Pfeiffer, L. Pompili, and A. Toubiana, (2024), [arXiv:2404.05811 \[gr-qc\]](#).
- [12] A. Gupta *et al.*, (2024), [arXiv:2405.02197 \[gr-qc\]](#).
- [13] L. Pompili, A. Buonanno, and M. Pürrer, (2024), [arXiv:2410.16859 \[gr-qc\]](#).
- [14] R. Bachhar, M. Pürrer, and S. R. Green, (2024), [arXiv:2410.17168 \[gr-qc\]](#).
- [15] R. S. Chandramouli, K. Prokup, E. Berti, and N. Yunes, (2024), [arXiv:2410.06254 \[gr-qc\]](#).
- [16] P. Amaro-Seoane *et al.* (LISA), (2017), [arXiv:1702.00786 \[astro-ph.IM\]](#).
- [17] M. Colpi *et al.* (LISA), (2024), [arXiv:2402.07571 \[astro-ph.CO\]](#).
- [18] E. Berti, *Class. Quant. Grav.* **23**, S785 (2006), [arXiv:astro-ph/0602470](#).
- [19] C. Cutler and M. Vallisneri, *Phys. Rev. D* **76**, 104018 (2007), [arXiv:0707.2982 \[gr-qc\]](#).
- [20] D. Ferguson, K. Jani, P. Laguna, and D. Shoemaker, *Phys. Rev. D* **104**, 044037 (2021), [arXiv:2006.04272 \[gr-qc\]](#).
- [21] N. Afshordi *et al.* (LISA Consortium Waveform Working Group), (2023), [arXiv:2311.01300 \[gr-qc\]](#).
- [22] E. Berti, V. Cardoso, J. A. Gonzalez, U. Sperhake, M. Hannam, S. Husa, and B. Bruegmann, *Phys. Rev.*

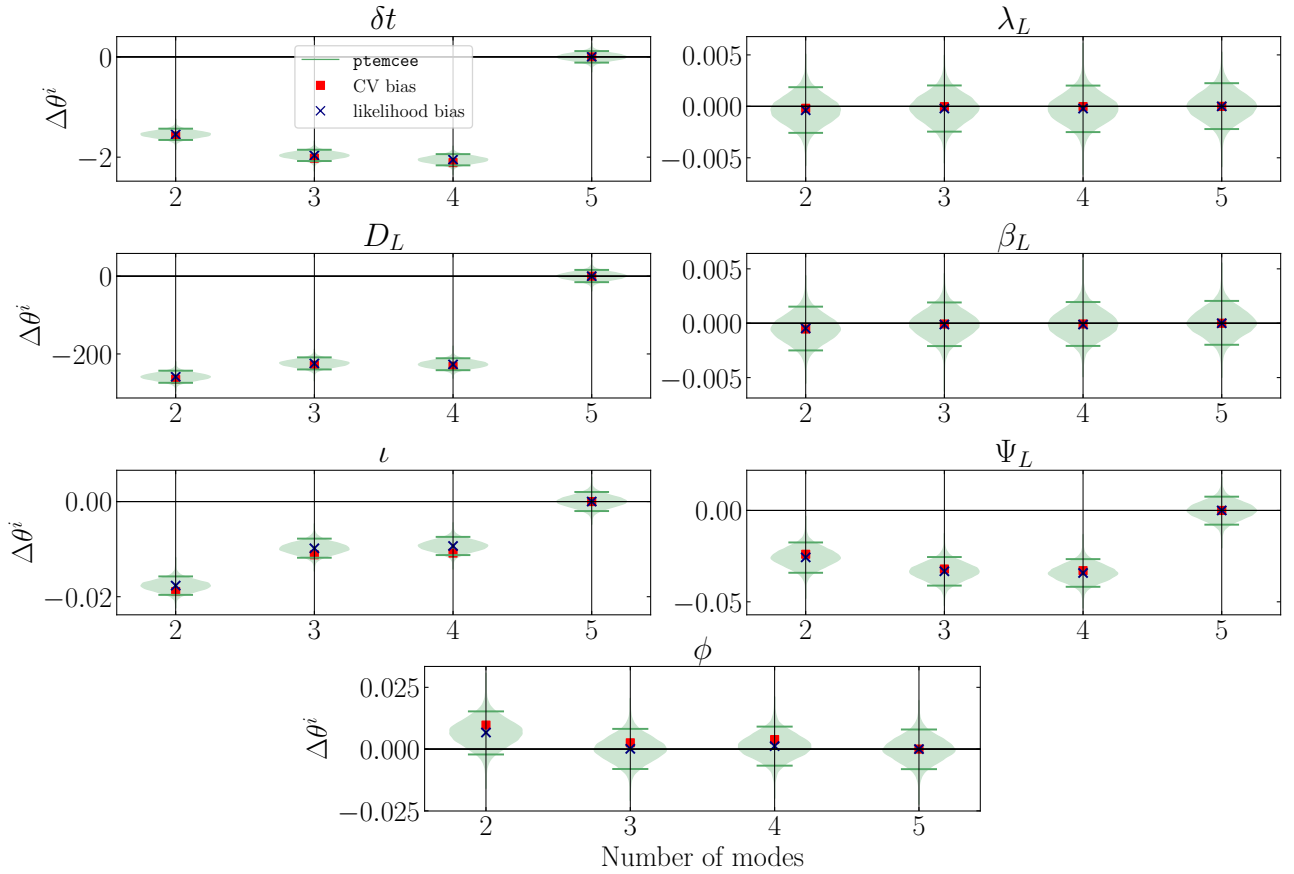


FIG. 20. Systematic bias on extrinsic parameters estimated within the linear signal approximation (“CV bias”) and with the direct optimization method (“likelihood bias”) compared to biases recovered in full PE (“`ptemcee`”). Results are shown for the $M = 10^6 M_\odot$, $q = 8$, $\iota = \pi/12$ event also discussed in Sec. V.

- D **76**, 064034 (2007), arXiv:gr-qc/0703053.
- [23] V. Baibhav, E. Berti, V. Cardoso, and G. Khanna, *Phys. Rev. D* **97**, 044048 (2018), arXiv:1710.02156 [gr-qc].
- [24] V. Baibhav and E. Berti, *Phys. Rev. D* **99**, 024005 (2019), arXiv:1809.03500 [gr-qc].
- [25] V. Baibhav, E. Berti, and V. Cardoso, *Phys. Rev. D* **101**, 084053 (2020), arXiv:2001.10011 [gr-qc].
- [26] V. Varma and P. Ajith, *Phys. Rev. D* **96**, 124024 (2017), arXiv:1612.05608 [gr-qc].
- [27] J. Calderón Bustillo, S. Husa, A. M. Sintes, and M. Pürrer, *Phys. Rev. D* **93**, 084019 (2016), arXiv:1511.02060 [gr-qc].
- [28] T. B. Littenberg, J. G. Baker, A. Buonanno, and B. J. Kelly, *Phys. Rev. D* **87**, 104003 (2013), arXiv:1210.0893 [gr-qc].
- [29] V. Varma, P. Ajith, S. Husa, J. C. Bustillo, M. Hannam, and M. Pürrer, *Phys. Rev. D* **90**, 124004 (2014), arXiv:1409.2349 [gr-qc].
- [30] P. B. Graff, A. Buonanno, and B. S. Sathyaprakash, *Phys. Rev. D* **92**, 022002 (2015), arXiv:1504.04766 [gr-qc].
- [31] F. H. Shaik, J. Lange, S. E. Field, R. O’Shaughnessy, V. Varma, L. E. Kidder, H. P. Pfeiffer, and D. Wysocki, *Phys. Rev. D* **101**, 124054 (2020), arXiv:1911.02693 [gr-qc].
- [32] P. T. H. Pang, J. Calderón Bustillo, Y. Wang, and T. G. F. Li, *Phys. Rev. D* **98**, 024019 (2018), arXiv:1802.03306 [gr-qc].
- [33] I. Harry, J. Calderón Bustillo, and A. Nitz, *Phys. Rev. D* **97**, 023004 (2018), arXiv:1709.09181 [gr-qc].
- [34] J. Calderón Bustillo, P. Laguna, and D. Shoemaker, *Phys. Rev. D* **95**, 104038 (2017), arXiv:1612.02340 [gr-qc].
- [35] D. A. Brown, P. Kumar, and A. H. Nitz, *Phys. Rev. D* **87**, 082004 (2013), arXiv:1211.6184 [gr-qc].
- [36] D. Wadekar, J. Roulet, T. Venumadhav, A. K. Mehta, B. Zackay, J. Mushkin, S. Olsen, and M. Zaldarriaga, (2023), arXiv:2312.06631 [gr-qc].
- [37] D. Wadekar, T. Venumadhav, A. K. Mehta, J. Roulet, S. Olsen, J. Mushkin, B. Zackay, and M. Zaldarriaga, *Phys. Rev. D* **110**, 084035 (2024), arXiv:2310.15233 [gr-qc].
- [38] D. Wadekar, T. Venumadhav, J. Roulet, A. K. Mehta, B. Zackay, J. Mushkin, and M. Zaldarriaga, *Phys. Rev. D* **110**, 044063 (2024), arXiv:2405.17400 [gr-qc].
- [39] A. K. Mehta, D. Wadekar, J. Roulet, I. Anantpurkar, T. Venumadhav, J. Mushkin, B. Zackay, M. Zaldarriaga, and T. Islam, (2025), arXiv:2501.17939 [gr-qc].
- [40] C. Pitte, Q. Baghi, S. Marsat, M. Besançon, and A. Petiteau, *Phys. Rev. D* **108**, 044053 (2023), arXiv:2304.03142 [gr-qc].
- [41] S. Marsat, J. G. Baker, and T. Dal Canton, *Phys. Rev. D* **103**, 083011 (2021), arXiv:2003.00357 [gr-qc].
- [42] C. García-Quirós, M. Colleoni, S. Husa, H. Estellés, G. Pratten, A. Ramos-Buades, M. Mateu-Lucena, and R. Jaume, *Phys. Rev. D* **102**, 064002 (2020),

- arXiv:2001.10914 [gr-qc].
- [43] G. Pratten, S. Husa, C. Garcia-Quiros, M. Colleoni, A. Ramos-Buades, H. Estelles, and R. Jaume, *Phys. Rev. D* **102**, 064001 (2020), arXiv:2001.11412 [gr-qc].
- [44] S. Babak, A. Petiteau, and M. Hewitson, (2021), arXiv:2108.01167 [astro-ph.IM].
- [45] S. Marsat and J. G. Baker, (2018), arXiv:1806.10734 [gr-qc].
- [46] W. D. Vousden, W. M. Farr, and I. Mandel, *Mon. Not. Roy. Astron. Soc.* **455**, 1919 (2016), arXiv:1501.05823.
- [47] D. Foreman-Mackey, D. W. Hogg, D. Lang, and J. Goodman, *Publ. Astron. Soc. Pac.* **125**, 306 (2013), arXiv:1202.3665 [astro-ph.IM].
- [48] J. Goodman and J. Weare, *Commun. Appl. Math. Comput. Sc.* **5**, 65 (2010).
- [49] A. Antonelli, O. Burke, and J. R. Gair, *Mon. Not. Roy. Astron. Soc.* **507**, 5069 (2021), arXiv:2104.01897 [gr-qc].
- [50] J. A. Nelder and R. Mead, *Comput. J.* **7**, 308 (1965).
- [51] P. Virtanen, R. Gommers, T. E. Oliphant, M. Haberland, T. Reddy, D. Cournapeau, E. Burovski, P. Peterson, W. Weckesser, J. Bright, S. J. van der Walt, M. Brett, J. Wilson, K. J. Millman, N. Mayorov, A. R. J. Nelson, E. Jones, R. Kern, E. Larson, C. J. Carey, Í. Polat, Y. Feng, E. W. Moore, J. VanderPlas, D. Laxalde, J. Perktold, R. Cimrman, I. Henriksen, E. A. Quintero, C. R. Harris, A. M. Archibald, A. H. Ribeiro, F. Pedregosa, P. van Mulbregt, and SciPy 1.0 Contributors, *Nat. Methods* **17**, 261 (2020), arXiv:1907.10121 [cs.MS].
- [52] L. London, S. Khan, E. Fauchon-Jones, C. García, M. Hannam, S. Husa, X. Jiménez-Forteza, C. Kalaghatgi, F. Ohme, and F. Pannarale, *Phys. Rev. Lett.* **120**, 161102 (2018), arXiv:1708.00404 [gr-qc].
- [53] C. K. Mishra, A. Kela, K. G. Arun, and G. Faye, *Phys. Rev. D* **93**, 084054 (2016), arXiv:1601.05588 [gr-qc].
- [54] S. Yi *et al.*, in preparation.